CrossMark

JM PAPERS

Cross-shore wind-induced changes to field-scale overturning wave shape

Falk Feddersen[1],†, Adam M. Fincham[2,3,4], Katherine L. Brodie[5], Adam P. Young[1], M.S. Spydell[1], Derek J. Grimes[6], Michal Pieszka[2,3] and Kentaro Hanson[1]

[1]Scripps Institution of Oceanography, UCSD, La Jolla, CA 92093, USA

[2]World Surf League, Los Angeles, CA 90405, USA

[3]Kelly Slater Wave Company, Los Angeles, CA 90405, USA

[4]Department of Aerospace and Mechanical Engineering, University of Southern California, Los Angeles, CA 90089, USA

[5]US Army Engineer Research and Development Center, Coastal and Hydraulics Laboratory, Duck, NC 97949, USA

[6]University of North Carolina Wilmington, Wilmington, NC 28403, USA

The shape of depth-limited breaking-wave overturns is important for turbulence injection, bubble entrainment and sediment suspension. Overturning wave shape depends on a nonlinearity parameter H/h, where H is the wave height, and h is the water depth. Cross-shore wind direction (offshore/onshore) and magnitude affect laboratory shoaling wave shape and breakpoint location X_{bp}, but wind effects on overturning wave shape are largely unstudied. We perform field-scale experiments at the Surf Ranch wave basin with fixed bathymetry and ≈ 2.25 m shoaling solitons with small height variations propagating at $C = 6.7$ m s^{-1}. Observed non-dimensional cross-wave wind U_w was onshore and offshore, varying realistically ($-1.2 < U_w/C < 0.7$). Georectified images, a wave staff, and lidar are used to estimate X_{bp}, H/h, overturn area A and aspect ratio for 22 waves. The non-dimensionalized X_{bp} was inversely related to U_w/C. The non-dimensional overturn area and aspect ratio also were inversely related to U_w/C, with smaller and narrower overturns for increasing onshore wind. No overturning shape dependence on the weakly varying H/h was seen. The overturning shape variation was as large as prior laboratory experiments with strong H/h variations without wind. An idealized potential air flow simulation on steep shoaling soliton shape has strong surface pressure variations, potentially inducing overturning shape changes. Through wave-overturning

† Email address for correspondence: ffeddersen@ucsd.edu

958 A4-1

impacts on turbulence and sediment suspension, coastal wind variations could be relevant for near-shore morphology.

Key words: air/sea interactions, wind-wave interactions, solitary waves

1. Introduction

The depth-limited breaking of surface gravity waves is a beautiful and majestic phenomenon. Wave breaking occurs when Eulerian fluid velocity u within the wave exceeds the wave phase speed C (e.g. Derakhti *et al.* 2020; Varing *et al.* 2021), typically leading to wave overturning and subsequently the wave jet impacting the sea surface in front of the wave. Wave breaking is often categorized into spilling and plunging breaking (e.g. Peregrine 1983), where spilling waves have very small overturns, and plunging waves have larger overturns. However, this categorization is qualitative and often identified by sight. In laboratory and field observations, the shape of the wave overturn is important in setting the size of the resulting splash up and bubble entrainment (Chanson & Jaw-Fang 1997; Yasuda *et al.* 1999; Blenkinsopp & Chaplin 2007), water column turbulence (Ting & Kirby 1995, 1996; Aagaard, Hughes & Ruessink 2018), sediment suspension (Voulgaris & Collins 2000; Aagaard *et al.* 2018) and wave impact forces on engineered structures (Bullock *et al.* 2007), which may also apply to coastal cliffs (Thompson, Young & Dickson 2019). Similarly, in numerical simulations of deep-water and depth-limited wave breaking, the geometry of wave-overturning impacts air entrainment, vorticity generation and pathways of turbulent dissipation (e.g. Lubin *et al.* 2006; Derakhti & Kirby 2014; Deike, Melville & Popinet 2016; Mostert & Deike 2020). Thus understanding the factors that affect the shape of overturning waves is important to a range of processes. Surfers have long understood that offshore (blowing from shore to sea) wind results in larger and more square (1 : 1 aspect ratio) overturns relative to onshore (blowing from sea to shore) wind. Yet this effect of cross-shore wind on overturning wave shape has largely been unstudied. Here, we examine the effect of onshore and offshore wind on field-scale overturning wave shape.

As waves shoal, the shallow-water nonlinearity parameter H/h increases, where H is the wave height, and h is the water depth. In addition, shoaling waves change shape, becoming steeper with narrower peaks (i.e. skewness) and more pitched forward (i.e. asymmetry) before overturning and breaking (Elgar & Guza 1985). The nonlinearity parameter is well understood to strongly affect the location of wave breaking (e.g. McCowan 1894; Thornton & Guza 1983). Wave-overturn shape has been quantified with its area A and its aspect (width to length) ratio W/L (Mead & Black 2001), which are known to depend on bathymetric parameters (such as β, the bathymetric slope) and local nonlinearity parameters (H/h). The parameters A, W and L are defined in § 3. In laboratory planar slope settings, β is well understood to be important in setting spilling or plunging wave breaking via the Iribarren number (e.g. Peregrine 1983). Similarly, β is also important in setting the overturning wave shape. On a planar beach with β varying from 0.01 to 0.067, nearly exact potential flow boundary element model (BEM) solutions reveal that wave-overturn area A increases with β for fixed initial soliton amplitude (Grilli, Svendsen & Subramanya 1997). Similar changes to overturn area were also evident with incident solitons on a planar beach in two-phase direct numerical simulations (DNS) modelling with β from 0.018 to 0.052 (Mostert & Deike 2020). Field observations of wave overturns with random waves

over a barred beach bathymetry also observed increasing non-dimensional wave-overturn area A/H_b^2 (where H_b is the breaking wave height) for larger local β varying from 0.02 to 0.026 (O'Dea, Brodie & Elgar 2021). The overturn aspect ratio W/L was found to depend somewhat on local $\beta/(kh)$, where kh is the non-dimensional depth based on a peak wavenumber k (O'Dea *et al.* 2021).

Wave-overturn shape also depends on the local nonlinearity parameter H/h, particularly on bars or reefs that have minimum depth at the top of the bar or reef. In BEM simulations of a soliton incident on a step reef (i.e. no slope), the wave-overturn area increased for shallower reefs (larger steps) (Yasuda, Mutsuda & Mizutani 1997). Blenkinsopp & Chaplin (2008) examined overturning wave shape for laboratory progressive waves over a triangular bathymetry with constant β but variable shallowest depth h_c that immediately farther shoreward falls off to deeper water. Non-dimensional wave-overturn area A/H_b^2 was proportional to a nonlinearity parameter H_0/h_c where H_0 was an deep-water wave height, qualitatively consistent with the step reef of Yasuda *et al.* (1997). For the triangular bathymetry, no relationship was evident between overturn aspect ratio W/L and nonlinearity parameter H_0/h_c (Blenkinsopp & Chaplin 2008).

Wind blowing over surface gravity waves leads to wave growth and decay (e.g. Miles 1957; Phillips 1957), but can also change the wave shape in both deep (Leykin *et al.* 1995; Zdyrski & Feddersen 2020) and shallow (Zdyrski & Feddersen 2021) water. Few studies have examined the combined effect of wind and shoaling effects. In laboratory studies, onshore wind results in wave breaking in deeper water (Douglass 1990) and decreases H/h at breaking (King & Baker 1996), with the opposite for offshore wind. Numerical studies using two-phase Reynolds-averaged Navier–Stokes (RANS) solvers of wind-forced solitary (Xie 2014) and progressive (Xie 2017) waves have found results similar to aspects of these laboratory experiments. A parametrized wind energy input within a wave-averaged model can reproduce the changes in wave breakpoint location and H/h at breaking (Sous *et al.* 2021). In a laboratory experiment, Feddersen & Veron (2005) demonstrated that stronger onshore wind enhanced the temporal-wave shape (asymmetry) of shoaling waves. Similar wind effects on laboratory shoaling wave skewness and asymmetry were also observed recently (Sous *et al.* 2021). Zdyrski & Feddersen (2022) derived a variable coefficient KdV–Burgers equation for a wind-forced soliton shoaling on a planar slope using the Jeffreys (1925) mechanism. Solving this equation numerically, wind direction and speed changed the polarity and magnitude of the induced bound dispersive tail, resulting in wave-shape changes focused on the rear wave face (Zdyrski & Feddersen 2022), qualitatively consistent with Feddersen & Veron (2005). However, this study was limited to shoaling well before wave overturning due to the asymptotic limits of the derivation. As normal-stresses (pressure) increase for steeper open-ocean waves, wind-induced effects would likely be even larger for waves near breaking. However, the effects of wind on overturning wave shape have been poorly studied at field scales, due to the difficulties of isolating other influential environment parameters, such as tides, bathymetry, and random and directionally spread wave fields from wind effects. For example, in one field study with natural bathymetric and wave field variations, cross-shore wind was weakly correlated to the overturn aspect ratio, with offshore (onshore) wind increasing (reducing) the aspect ratio (O'Dea *et al.* 2021). However, wind variation was relatively weak, and co-variation with other parameters was not considered. Here, we examine the dependence of the non-dimensional wave-overturn area and aspect ratio on non-dimensional cross-shore wind speed U_w/C, where C is the wave phase speed,

and U_w/C is positive for onshore wind. Specifically, we hypothesize larger (smaller) non-dimensional area A/H^2 and aspect ratio W/L for increasing offshore (onshore) winds.

Prior to the field study of O'Dea *et al.* (2021), quantitative wave-overturn shape studies were based on laboratory experiments (e.g. Blenkinsopp & Chaplin 2008). The rapid transformation of field-scale shoaling to overturning waves requires high temporal and spatial resolution measurements. Advances in using lidar (light detection and ranging) technology to measure surface gravity waves directly (e.g. Brodie *et al.* 2015; Martins *et al.* 2017, 2018; Carini, Chickadel & Jessup 2021) provide such high-resolution measurements of field-scale waves. Here, we isolate the effect of cross-wave wind on overturning wave shape for field-scale waves on a fixed bathymetry with small variation in incident waves. These observations were made at the Kelly Slater Wave Company's Surf Ranch – a wave basin designed for surfing and used here as a laboratory. In § 2, we describe the fixed bathymetry and waves of the basin, and detail the instrumentation deployed. Analysis methods are detailed in § 3, particularly estimation of wave-overturning parameters. Although coastal wind can blow in any direction relative to wave propagation, we focus on the component of wind in the direction of wave propagation, typically cross-shore (i.e. onshore or offshore) wind. In the results (§ 4), we examine the effect of cross-wave wind on wave breakpoint location, wave-overturn area and aspect ratio, while concurrently examining the effect of a nonlinearity parameter. The context of our results, limitations of our observations, potential mechanisms and implications are discussed in § 5. Section 6 provides a summary.

2. Methods

2.1. *Description of the Surf Ranch wave basin*

The Surf Ranch wave basin, located in Lemoore, CA, USA, is oriented nearly north to south and is approximately 600 m long and 60 m wide (figure 1*a*). The bed of the wave basin is fixed (i.e. not mobile). The western side of the basin has a sloping beach. On the eastern side of the basin, northbound and southbound waves are generated by a submerged hydrofoil towed along-basin on a tram. We define a cross- and along-basin (x, y) coordinate system, with $(x, y) = (0, 0)$ located at the centre of the study region, where an instrument frame called 'the rig' was deployed (figure 1, black dot). The wave basin bathymetry has a deep flat region on the east side, and shallows towards the west. The bathymetry profile varies along-basin to provide variation in surfing experience. However, in the central study region of the wave basin ($-35 < y < 35$ m), the bathymetry is along-basin uniform and varies only cross-basin (figure 1*b*). In the region where waves are generated ($x > 18$ m), the bathymetry is flat with still water depth $h \approx 2.5$ m. A relatively steep sloping section begins at $x \approx 13$ m, which transitions to a flat bar at $x \approx 3$ m that is approximately 6 m wide with $h \approx 0.95$ m (figure 1*d*). Shoreward of the bar is a deeper trough that then transitions into a beach slope even farther shoreward (figure 1*d*). The bathymetry is designed so that wave overturning occurs on the bar (figure 1), allowing surfers the opportunity to get 'tubed' and allowing for the study of field-scale overturning wave shape.

The hydrofoil is pulled along-basin in a supercritical regime by the tram, generating an approximate soliton with wave height $H \approx 2$ m together with trailing dispersive waves (figure 1). The soliton propagates at an angle of $25.5°$ to the hydrofoil. Thus, from the perspective of the shoreline, the solitons are highly obliquely ($\approx 65°$) incident. The solitons propagate up the slope and overturn on the bar (figure 1*b,c*). Under slowly varying bathymetric conditions, the soliton phase speed would be tied to the wave height and
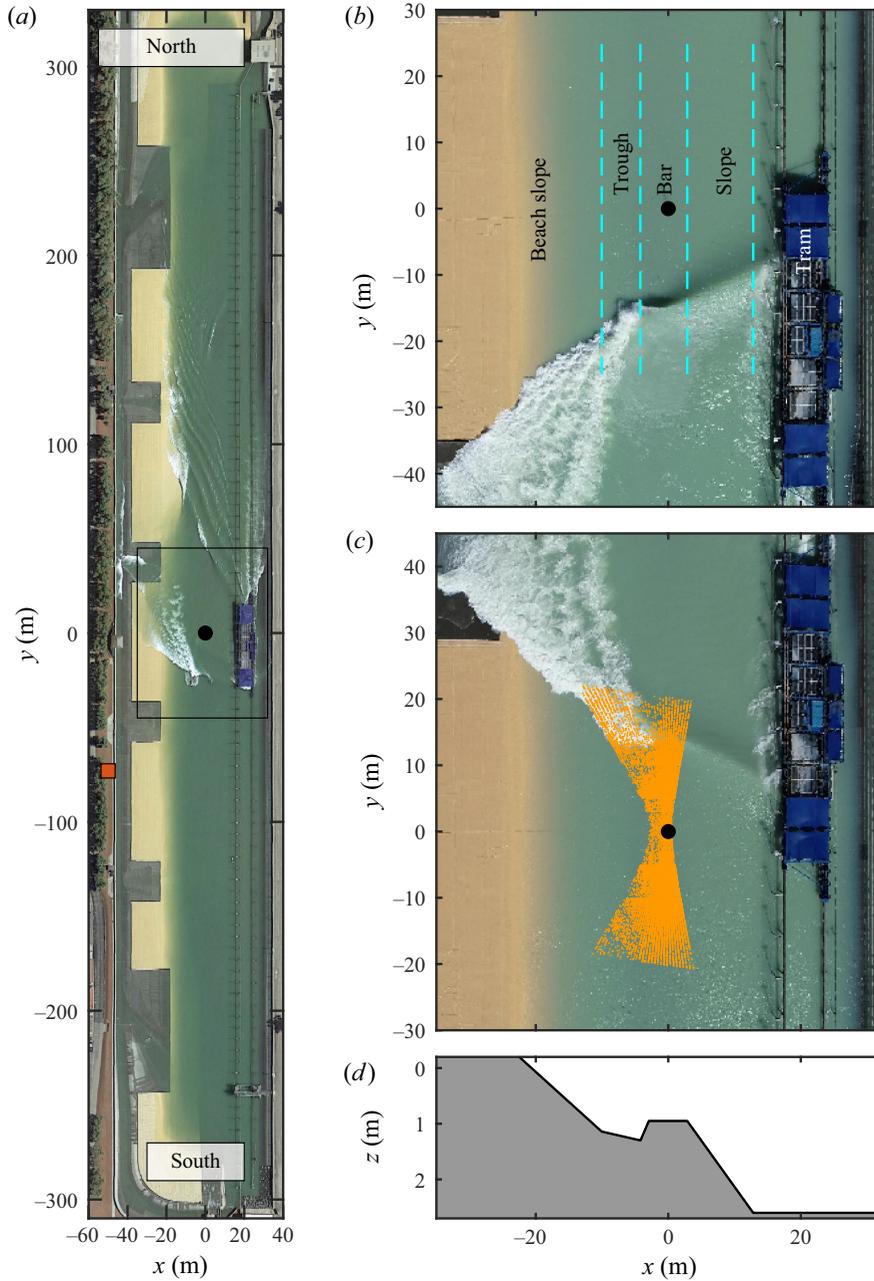
Figure 1. Overview of the Kelly Slater Wave Company's Surf Ranch wave basin. (*a*) Aerial photo showing the entire basin in Surf Ranch (x, y) coordinates, with north and south indicated. The black dot shows the location of the rig at $(x, y) = (0, 0)$ m, and the orange square shows the location of the meteorological station at $(x, y) = (-50, -73)$ m. The thin black rectangle indicates the centre region of the basin shown in (*b,c*). (*b*) Georectified unmanned aerial vehicle (UAV) image of the centre region with a right-wave generated by the submerged hydrofoil towed along-basin by the tram. Bathymetry contours delineate slope, bar, trough and beach slope regions. (*c*) Georectified UAV image of the centre region with a left-wave. Orange dots indicate subsampled coverage of the Velodyne HDL-32 lidar. (*d*) Cross-basin transect of Surf Ranch bathymetry at $y = 0$.

water depth. However, the depth varies rapidly relative to the soliton full width ≈ 6 m. Projected into the direction of propagation, the water depth is halved over 16 m. The ratio of soliton full width to bathymetric variation distance is 0.38, which is not $\ll 1$. Thus a slowly-varying paradigm does not hold, and the soliton does not have a chance to refract prior to wave overturning. This results in a straight wave crest even though the water depth varies (figure 1*b,c*). A similar lack of wave refraction over rapidly varying two-dimensional bathymetry was evident in the two-dimensional overturning wave modelling (Guyenne & Grilli 2006). When the hydrofoil is northbound, it generates a northward propagating wave (figure 1*b*), which from the perspective of an observer (surfer) looking in the direction of wave propagation has open (non-breaking) wave face to the right. Similarly, with the southbound hydrofoil, propagating waves are generated with open face to the left (figure 1*c*). Here, this surfing convention of right-wave and left-wave will be used to denote northward and southward propagating waves, respectively.

The observation period occurred in March 2019, including the afternoon of 12 March, the afternoon of 13 March, and the morning of 14 March. No surfing occurred during these times. During the observation period, the hydrofoil was pulled at different speed profiles to generate different surfing wave types. Here, we focus on waves that were generated with the same hydrofoil speed profile – denoted CT3 – that had a constant along-basin speed $C_y \approx 7.4$ m s^{-1} in the study region $-35 < y < 35$ m (figures 1*b,c*). A basin seiche is induced by the wave generation and breaking. As such, there were intervals of 3–8 min between wave generation, allowing the seiche to reduce. Subtle hydrofoil variations for northbound and southbound waves result in left- and right-waves being slightly different. The hydrofoil was also slightly modified prior to generating waves on 14 March, resulting in slightly larger waves. Thus with seiche, left-wave and right-wave variations, and hydrofoil variations, the CT3 generated waves are not all identical and we must be careful to isolate the effects of cross-wave wind against nonlinearity (variation in the size of generated waves) and bathymetric (seiching changing the depth of the bar) induced changes to overturning wave shape.

2.2. *Instrumentation and data*

2.2.1. *Ground-based images*
At each end of the wave basin, an automated camera system takes video of each wave, from which we extract still images. These images provide qualitative information about each wave. Example images of a left- and right-wave approaching $(x, y) = (0, 0)$ m are shown in figures 2(*a,b*).

2.2.2. *UAV-based images*
A DJI Phantom 4 Pro unmanned aerial vehicle (UAV) was used to take videos of the waves as they pass the rig. The UAV was flown at elevation 120 m above the water surface. Videos were taken in 4K (3840 by 2160 pixels at 30 frames per second). Images were extracted from the videos at 5 Hz centred on the rig, georectified using a flat plane at the still-water elevation in NAVD88 using multiple ground-control points following Bruder & Brodie (2020), and put into the (x, y) coordinate system (figures 1*b,c* and 2*e,f*). Georectified images have spatial resolution $(\Delta x, \Delta y) \approx 0.05$ m.
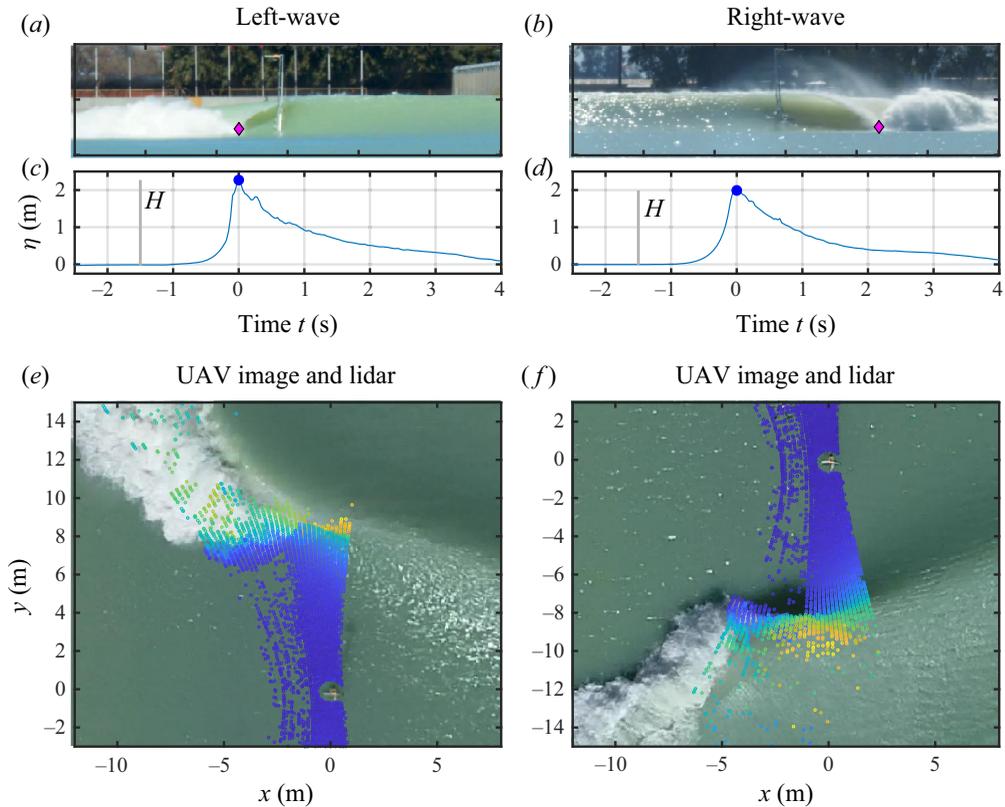
Figure 2. Overview of (a,c,e) a left-wave and (b,d,f) a right-wave. (a,b) Ground-based photograph of oncoming wave just prior to arrival at the rig (vertical pole extending from the water). The magenta diamond indicates the approximate breakpoint location where the overturning lip impacts the wave face, resulting in a splash up. (c,d) Wave staff water level η versus time t. The blue circle represents the maximum of η, and the vertical grey bar represents the wave staff wave height H. Note that the mean pre-wave water levels were -0.03 m and -0.007 m, respectively. (e,f) Georectified aerial image in (x, y) coordinates as the wave is approaching the rig at $(x, y) = (0, 0)$ m, with overlaid lidar returns (colour indicates elevation, no scale).

2.2.3. *Wave staff deployed at rig*

A tripod (denoted the 'rig') was deployed at $(x, y) = (0, 0)$ about 20 m from the mean shoreline in the centre of the flat bar region (black dot in figure 1b). The still-water level at the tripod is on average 0.95 m. An Ocean Sensor Systems OSSI-010-025 Wave Staff XB was mounted on the tripod that sampled at 32 Hz and communicated over a wireless network with occasional drop outs. The wave staff is calibrated so that the still-water depth is known. Only waves with wave staff data were included in the analysis. Based on image data, waves that were clearly broken prior to encountering the wave staff were not included. Time series of wave staff water level $\eta(t)$ characteristically have a rapidly growing front face and a slower receding back face consistent with shoaling-induced increase in wave asymmetry (figures 2c,d). Wave arrival times were estimated as the first maximum in the wave staff data (see blue circle in figure 2c,d). For each wave, pre-wave water levels are estimated from a 1 s-long time average of $\eta(t)$, from 3.75 s to 2.75 s prior to wave arrival. The wave height H is estimated as η at the arrival time minus the pre-wave water level (grey bars in figures 2c,d). The pre-wave water depth h is the pre-wave water level plus the still-water depth.

2.2.4. *Lidar deployed at rig*

Three-dimensional snapshots of the water surface are generated with a Velodyne HDL-32 lidar that was deployed on top of a vertical pole attached to the rig at $(x, y) = (0, 0)$ m at elevation 4.05 m above the still-water surface. The HDL-32 lidar has 32 beams with 903 nanometre wavelength scanning at 10 Hz, and was configured similar to that of O'Dea *et al.* (2021). Lidar returns from this sensor have a typical accuracy of ± 0.02 m. The lidar is oriented largely in the y direction to map the front face of the wave as it shoals and overturns (figure 1*c*). For a typical single wave, the (x, y) extent of all lidar returns ranges up to ± 20 m from the rig (figure 1*c*). The 32 lidar beams are spaced at 1.33° increments, yielding a 41° field of view. Thus the cross-basin extent of the scans increases with along-basin distance from the lidar, from ≈ 5 m at $|y| = 5$ m to ≈ 13 m at $|y| = 15$ m (figure 1*c*). Similarly, the cross-basin resolution varies from $\Delta x \approx 0.12$ m at $|y| = 5$ m to $\Delta x \approx 0.4$ m at $|y| = 15$ m. The azimuthal (along-basin) resolution is very high at 0.166°, equivalent to $\Delta y \approx 0.01$ m at $|y| = 15$ m. The extent of quality returns depends on the incident beam angle to the water surface, distance from the lidar, water roughness, and foam. As the lidar rotates 360° at 10 Hz, a snapshot of the wave is obtained over 0.1 s. Example lidar snapshots for a left- and right-wave are consistent with drone-based image observations (figures 2*e*,*f*).

2.2.5. *Wind measurements*

An AIRMAR PB100 meteorological station was mounted at elevation 16 m above the still-water level on the beach side just outside the basin at $(x, y) = (-50, -73)$ m (orange square in figure 1*a*). The cross- and along-basin winds in the (x, y) coordinate system (u_w, v_w) were sampled at 1 Hz, with occasional gaps interpolated linearly. Wind time series were then low-pass filtered with a 0.033 Hz cutoff frequency. On 12 and 13 March, the winds were mostly from the north-northwest (i.e. $u_w > 0$ and $v_w < 0$) at speeds generally 3–7 m s^{-1}. On 14 March, the winds were weaker (between 0.5–2 m s^{-1}) out of the south-southwest. For each wave, the wind values were estimated from the low-pass filtered wind at the rig wave arrival time (blue dot in figures 2*c*,*d*). No correction was made for the altitude of the wind measurements. Although a row of trees is present near the shore side of the wave basin in $-125 < y < 350$ m, we also assume no wind veering in the vertical. Analysis results are similar if only the along-basin component is used and the cross-basin component is set to zero.

3. Analysis

Here, we focus on the CT3 waves during the observational period that had data from the wave staff, UAV, Velodyne lidar and meteorological station. Occasionally, waves overturn and break at $x > 0$ (east of the wave staff), as determined from both ground-based and aerial images. These waves typically correspond to conditions when strong seiching was still present in the basin. Thus we also remove these waves from consideration, resulting in 22 total waves (11 left-waves and 11 right-waves).

3.1. *UAV image breakpoint*

The breakpoint location (x_{bp}, y_{bp}) is defined as where the overturning wave lip impacts the water surface creating a splash up of 'white water' (magenta diamonds in figures 2*a*,*b*). Breakpoint locations are identified by eye from georectified UAV images where the 'white
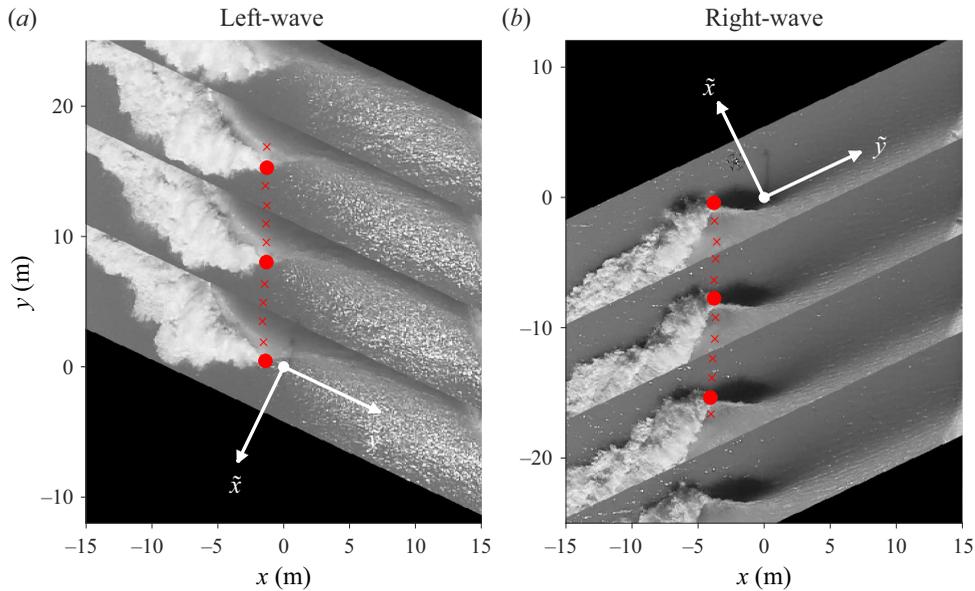
Figure 3. Breakpoints (x_{bp}, y_{bp}) (red markers) over UAV greyscale wave image slices for (*a*) the left-wave and (*b*) the right-wave shown in figure 2. Sequential image slices are at 1 Hz with associated (x_{bp}, y_{bp}) (solid red circles). The (x_{bp}, y_{bp}) at 5 Hz in between the 1 Hz images are denotes with red $\times$ symbols. Image slices are taken at $\pm 25.5°$ (right- and left-wave, respectively) with respect to x associated with the wave coordinate system $(\tilde{x}, \tilde{y})$ with origin $(\tilde{x}, \tilde{y}) = (0, 0)$ m also at the rig. Each individual image slice is 8 m wide in y and centred at y_{bp}.

water' splash origination location is clearly evident (figure 3). Breakpoint locations are determined within a 20 m along-basin region up-wave of the rig (at $(x, y) = (0, 0)$ m), so that any rig wake effects are not included. For a left-wave, the breakpoints (x_{bp}, y_{bp}) for four images, each separated by 1 s, are shown as solid red dots in figure 3(*a*), with the (x_{bp}, y_{bp}) from images in between indicated as red $\times$ symbols. Breakpoints for a right-wave are shown in figure 3(*b*). The x_{bp} vary weakly along-basin with variance 0.11 m^2 averaged over all 22 waves. For each wave, a single cross-basin breakpoint location X_{bp} is estimated as an along-basin average of x_{bp} for each y_{bp} located within 20 m up-wave of the rig, implying an averaging region $0 \leq y_{bp} \leq 20$ m or $-20 \leq y_{bp} \leq 0$ m for a left-wave or right-wave, respectively. As along-basin wave speeds are 7.4 m s^{-1}, and UAV images are at 5 Hz, the along-basin average X_{bp} includes 12 x_{bp} locations for each wave. The standard error of X_{bp} is 0.10 m, assuming independent estimates from each image. For all waves, X_{bp} is shoreward of the rig. The mean X_{bp} over all 22 waves is $\bar{X}_{bp} = -2.83$ m. For each wave, the perturbation cross-shore breakpoint is defined as $\Delta X_{bp} = X_{bp} - \bar{X}_{bp}$. The still-water shoreline is located at $x_{sl} = -20$ m. Thus the mean surf zone width (breakpoint distance from the mean shoreline) is $\bar{L}_{sz} = |\bar{X}_{bp} - x_{sl}|$, which is used to non-dimensionalize ΔX_{bp} in the results that follow.

3.2. *Visualizing wave overturns from lidar*

For analysis of wave overturns, each lidar snapshot is rotated into a wave coordinate system as in O'Dea *et al.* (2021), where $(\tilde{x}, \tilde{y})$ are in the wave propagation and along-wave directions, respectively, with $+\tilde{y}$ directed towards the tram where waves are generated,

and origin $(\tilde{x}, \tilde{y}) = (0, 0)$ m at the rig (see figure 3), which is also the origin of the (x, y) coordinate system. As discussed in § 2.1, the rapid bathymetric variations prevent soliton refraction, resulting in straight wave crests with a consistent angle of $25.5°$ relative to the x direction (figure 3). Thus, the $(\tilde{x}, \tilde{y})$ coordinate system is rotated $115.5°$ either clockwise (left-waves) or counter-clockwise (right-waves) from the (x, y) coordinate system. For right-waves, the $\tilde{y}$ axis is flipped (figure 3), resulting in a left-handed coordinate system. Thus both left- and right-waves have the breakpoint propagating in the $+\tilde{x}$ and $+\tilde{y}$ directions (figure 3). In the rotated wave coordinate system, left- and right-wave overturns are well captured by lidar snapshots (figure 4), as $-\tilde{y}$ directed views look directly into the overturn. For each wave, the wave coordinate system is fixed. Here, z is the vertical coordinate, with $z = 0$ m at the still-water level prior to the wave.

We highlight a few points for a left-wave and a right-wave as the waves propagate through the lidar field of view. For these obliquely incident waves (figures 2a,b), along-wave ($\tilde{y}$) variations from the wave face (larger $\tilde{y}$) to the overturn (smaller $\tilde{y}$) are visualized clearly (colours in figure 4). Here, the wave-overturn shape is quasi-uniform in time (snapshots, or successive rows in figure 4). As the wave propagates in the $+\tilde{x}$ direction, it also moves in the $+\tilde{y}$ direction (colours get darker in time, figure 4) as the wave breakpoint x_{bp} is essentially constant in y (figure 3). The density of lidar returns increases for smaller $|\tilde{x}|$ as the wave is closer to the rig, but the $\tilde{y}$ range (swath) also decreases (see also figure 1c). This left-wave is consistently at larger $\tilde{y}$ than the right-wave (figure 4) as the left-wave overturns at larger cross-basin x than the right-wave. Thus more of the wave face is visualized for the right-wave. Spray is observed clearly shedding off of the back of the right-wave (dots above $z = 2.5$ m, figure 4), which is not seen for the left-wave. The location of the mid-wave-face $\tilde{x}_{wf}$ is defined as the median $\tilde{x}$ for lidar returns at $0.95 < z < 1.05$ m. For each wave snapshot, the estimated $\tilde{x}_{wf}$ (grey diamonds in figure 4) represents well the $\tilde{x}$ location halfway up the wave face. To ensure sufficient lidar resolution and swath, we limit analysis of wave overturns to $\tilde{x}_{wf}$ between -8 m and -3 m.

The quasi-uniformity of the wave overturn across lidar snapshots (figure 4) together with the lack of soliton refraction (figures 1 and 3) implies that for a single snapshot, we can use the $\tilde{y}$ direction as a proxy for time. The along-basin hydrofoil (wave) speed $C_y = 7.4$ m s^{-1} and wave angle $25.5°$ yield $\tilde{x}$ wave propagation speed $C = 6.68$ m s^{-1} and $\tilde{y}$ propagation speed $C_{\tilde{y}} = 3.19$ m s^{-1}. Thus at a fixed time, moving an along-wave ($\tilde{y}$) distance 3.19 m is equivalent to 1 s of temporal wave evolution. A single lidar snapshot of the right-wave in figure 4 is binned in $\tilde{y}$ to demonstrate how the time evolution of wave overturning can be visualized (figure 5). Lidar returns are separated into $\Delta\tilde{y} = 2$ m wide bins, with bin-centres $\tilde{y}_c$ sliding over every 0.9 m varying from $\tilde{y}_c = -1.7$ m to -6.2 m (figure 5). The 4.5 m variation in $\tilde{y}_c$ corresponds to 1.4 s in time evolution, highlighting the rapid spatio-temporal evolution of such overturning waves. The $\Delta\tilde{y} = 2$ m bin width ensures a sufficient number of points for visualization, and contains 0.63 s of wave evolution. With this bin width, lidar returns can overlap across bins. Nearest the tram ($\tilde{y}_c = -1.7$ m, figure 5a), the wave face has not yet become vertical. Moving towards the overturn, the wave face is vertical at $\tilde{y}_c = -2.6$ m (figure 5b). At $\tilde{y}_c = -3.5$ m, the wave jet (lip) forms, ejecting forwards (figure 5c). At $\tilde{y}_c = -4.4$ m, the wave is overturning with jet falling forwards (figure 5d). At $\tilde{y}_c = -5.3$ m, the wave jet has fallen about 1.5 m in z and nearly makes contact with the water surface (figure 5e), about $+2$ m (in $\tilde{x}$) from where the wave became vertical. In this bin, most of the overturn surface (wave face, upper-back, bottom of
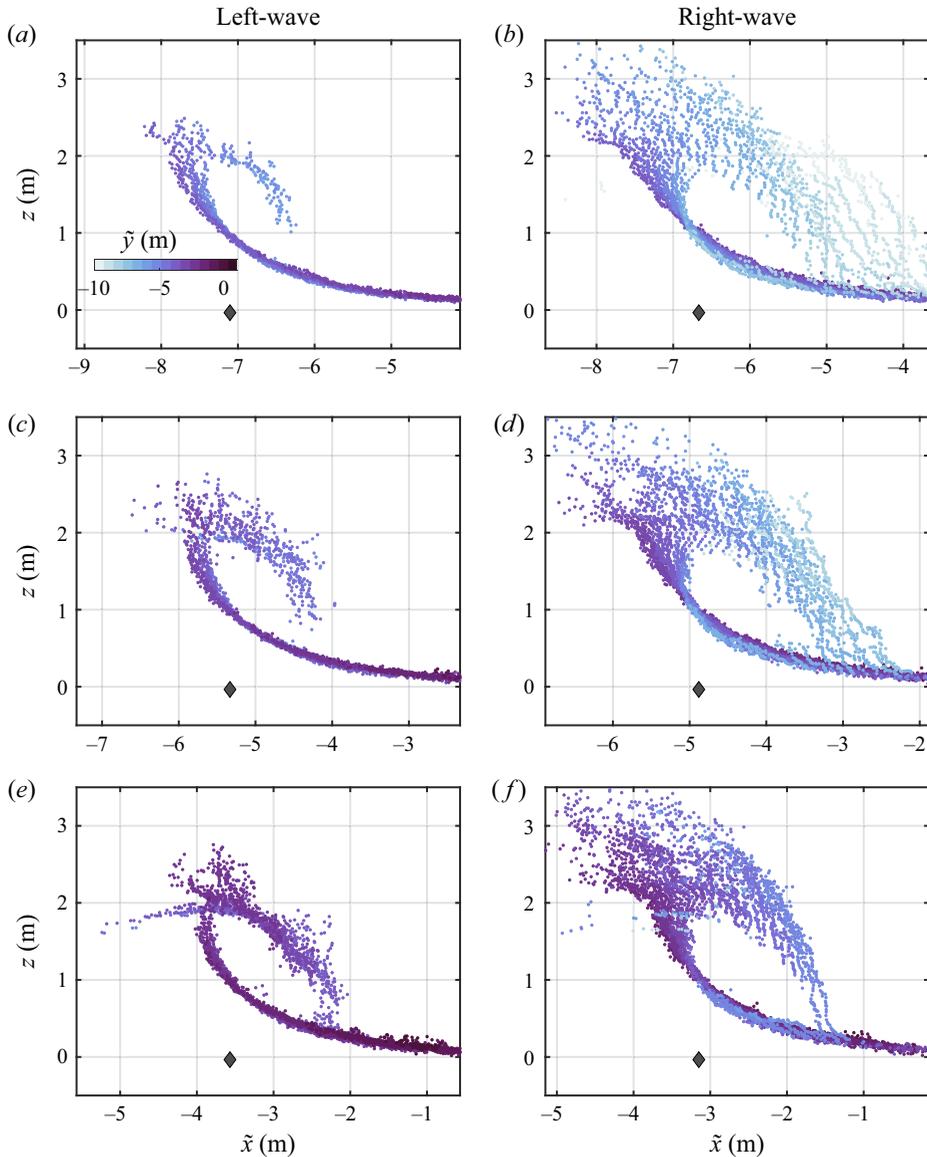
Figure 4. Visualizations of lidar snapshot returns in wave coordinates ($\tilde{x}$, z) of (*a*,*c*,*e*) the left-wave and (*b*,*d*,*f*) the right-wave shown in figures 2 and 3. The rows show three snapshots separated by 0.3 s each. Colours indicate along-wave distance $\tilde{y}$ as defined in figure 3. The grey diamonds indicate the mid-wave-face locations $\tilde{x}_{wf}$.

the jet) is visible. Farther shoreward at $\tilde{y}_c = -6.2$ m, the jet has impacted and the overturn surface is obscured from view (figure 5*f*).

3.3. *Projecting the wind vector into the wave propagation direction*

For each wave, the wind speed (U_w) in the direction of wave propagation was estimated as the dot product of the wind vector with the unit wave direction vector $\tilde{x}$ (figure 3). Thus $U_w < 0$ for offshore wind (in the opposite direction of wave propagation) and
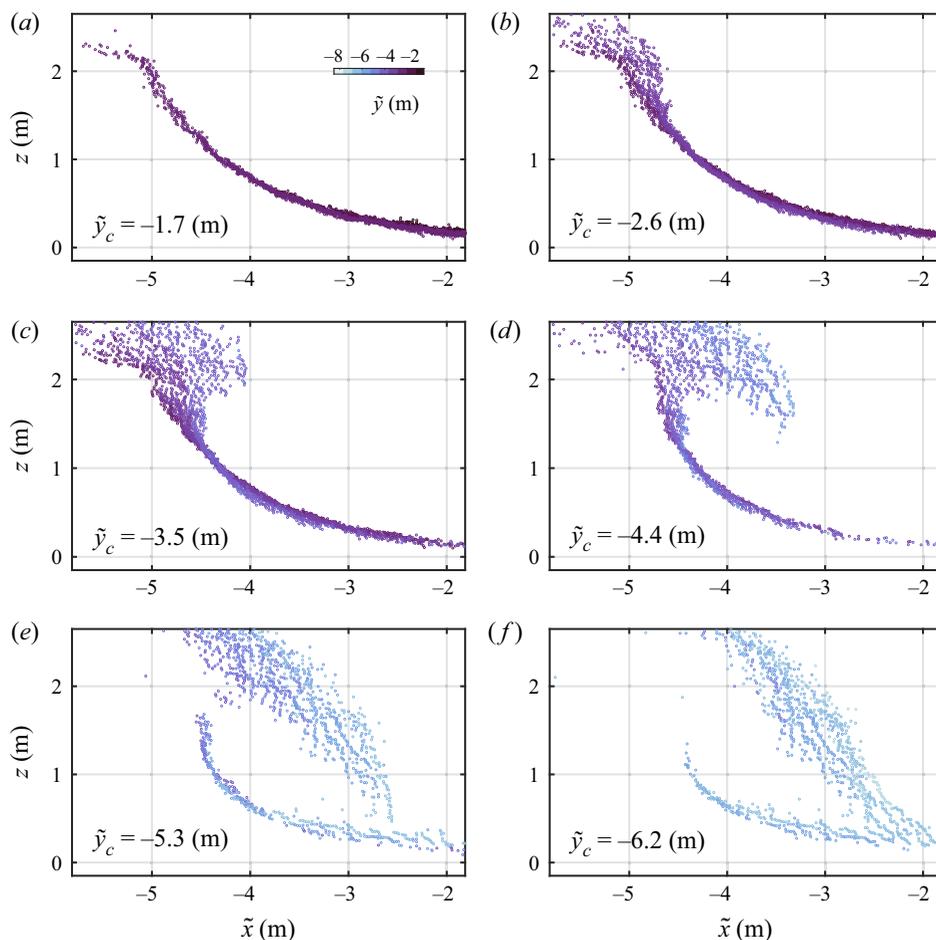
Figure 5. Visualizations of lidar snapshot returns in wave coordinates $(\tilde{x}, z)$ of the right-wave in figure 4 for $\Delta y = 2$ m wide bins at bin-centres $\tilde{y}_c$ separated by 0.9 m from (*a*) most positive $\tilde{y}_c$ (nearest wavemaker) to (*f*) most negative $\tilde{y}_c$ (nearest shoreline). The six panels cover 1.4 s of time evolution. Colours represent $\tilde{y}$. Each $\Delta y = 2$ m wide bin contains 0.63 s of time evolution.

$U_w > 0$ for onshore winds (in the direction of wave propagation). The non-dimensional wind speed in the direction of wave propagation U_w/C uses the wave speed in the direction of wave propagation $C = 6.68$ m s^{-1}, and will be used in subsequent analysis. The range of U_w/C spans from -1 to 0.7. This range can be contextualized by considering ocean waves breaking in $h = 2.5$ m depth. For such waves, $C \approx 5$ m s^{-1}, implying realistic cross-wave wind speed variation from -5 m s^{-1} to $+3.5$ m s^{-1}.

3.4. *Estimating wave-overturning shape parameters*

To extract overturn parameters such as area and aspect ratio, we fit lidar returns to a functional form representing an overturn. A parametric function based on cubic free-surface potential flow solutions (Longuet-Higgins 1982) is used to fit the shape of
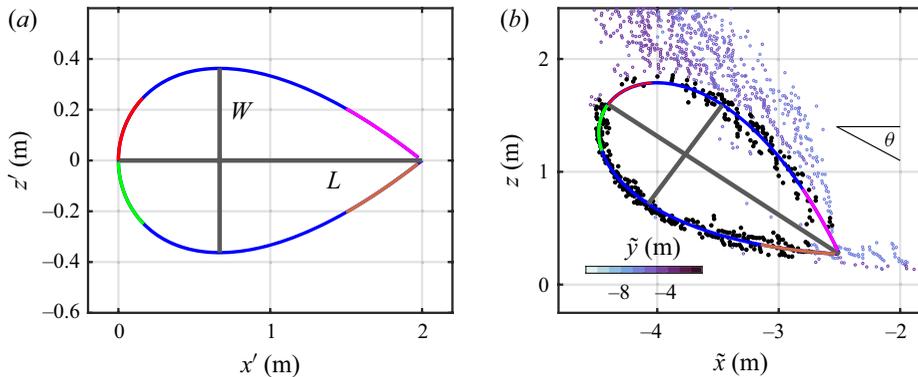
Figure 6. Schematic of overturn shape fitting. (*a*) The overturn curve from the Longuet-Higgins (1982) functional form (3.1) as a function of x' and z' for overturn length $L = 2$ m and width $W = 0.7258$ m, indicated with thick grey lines. Specific overturning regions are indicated in colour, including the upper-back (red) and lower-back (green) parts of the overturn at $x' \approx 0$, and at $x \approx L$, the overturning jet (magenta) impacting the water surface in front of the wave face (brown). (*b*) Example of the fitting method: lidar returns (coloured dots) as a function of $\tilde{x}$ and z of the $\Delta\tilde{y} = 2$ m region from figure 5 with the fit curve of (3.1). Black dots represent the fit-lidar returns. The thick grey lines represent the best fit $L = 2.32$ m and $W = 1.07$ m with other best-fit parameters $\theta = 35°$ (indicated in (*b*)), and $(\tilde{x}_0, z_0) = (-4.41, 1.60)$ m is the location of the back of the overturn. Note that the overturn has five fit-returns near the upper-back of the overturn (red), and ≥ 15 fit-returns in the jet (magenta) and front-face region (green), indicating that this is a fit-snapshot.

the wave overturn. The functional form is

$$\frac{z'}{W} = \pm \frac{3\sqrt{3}}{4} \sqrt{\frac{x'}{L}} \left(\frac{x'}{L} - 1 \right), \tag{3.1}$$

where the x' and z' coordinates are oriented along and across the overturn, and L and W are the overturn length and width, respectively (figure 6*a*). With (3.1), the region near $x' = 0$ is the back of the overturn (red and green, figure 6*a*), and the region near $x' = 2$ is where the overturning jet (magenta) intersects the water surface in front of the wave (brown). Parameters derived from W and L that will be analysed are the overturn area

$$A = \frac{2\sqrt{3}}{5} LW, \tag{3.2}$$

and the aspect ratio W/L. When rotated clockwise by an angle θ, the curve of the functional form (6*a*) is qualitatively similar to the shape of the overturn seen in figures 4 and 5. The functional form (3.1) has been used successfully to fit wave-overturning shape parameters from images of random waves breaking on reefs (Mead & Black 2001), laboratory visualizations of plunging waves (Blenkinsopp & Chaplin 2008), and field lidar observations of plunging breaking waves (O'Dea *et al.* 2021). As noted by O'Dea *et al.* (2021), (3.1) is only a potential flow solution when the overturn aspect ratio is $W/L = 0.36$ (Longuet-Higgins 1982). However, as pointed out by New (1983), this solution does not give the correct surface velocity for an overturn. Thus, as in previous work (Blenkinsopp & Chaplin 2008; O'Dea *et al.* 2021), the functional form (3.1) should be considered as means of quantifying wave-overturn shape and reducing it to two parameters, L and W.

For each lidar snapshot, we first select the $\Delta\tilde{y} = 2$ m wide binned region to fit to this functional form. We require the binned region to have returns that visualize most of the overturn surface and have the jet impacting or nearly impacting the water surface in front

of the wave. Such a binned region is denoted as having a complete overturn. Thus the binned regions in figures 5(*a–d*) do not qualify, as the jet is neither formed nor about to make impact. The binned region in figure 5(*f*) also does not qualify, as the back of the overturn (i.e. $(x', z') = (0, 0)$) is not visible. For this lidar snapshot, only the $\Delta \tilde{y} = 2$ m region shown in figure 5(*e*) qualifies as a candidate for fitting because it is the $\Delta \tilde{y}$ region with most positive $\tilde{y}_c$ with a complete overturn.

The method of fitting the lidar returns to (3.1) is similar that used by O'Dea *et al.* (2021) and illustrated in figure 6(*b*) for the binned lidar returns in figure 5(*e*). There are five fit parameters $(L, W, \theta, \tilde{x}_0, z_0)$, where θ is the clockwise rotation angle of the overturn major axis to the horizontal, and $(\tilde{x}_0, z_0)$ corresponds to $(x', z') = (0, 0)$, that is, the back of the overturn. The fit process is iterative. The first step is to fit all the binned lidar returns (coloured dots in figure 6*b*) to the parametric form of (3.1) yielding the first set of best-fit parameters. For the *i*th lidar return, d_i is defined as the minimum Euclidean distance from the lidar return to the fit-curve (3.1). The best-fit parameters are those that minimize the cost function of the mean square minimum distance averaged over all lidar returns $\langle d^2 \rangle$. This minimization is performed with a Nelder–Mead unconstrained simplex search method (Press *et al.* 1988; Lagarias *et al.* 1998). An initial parameter guess is needed, with L and W chosen larger than the largest overturn, $\theta = 40°$, and $(\tilde{x}_0, z_0)$ based on $\tilde{x}_{wf}$ and H. Next, as we seek to fit to lidar returns from the overturn surface, individual lidar returns are pruned based on their d_i values. Specifically, returns outside the curve with $d_i > 0.08$ m and returns inside the curve with $d_i > 0.4$ m are pruned. Remaining lidar returns are considered the fit returns. The fitting and pruning procedures are repeated using the previous best-fit parameters as initial guess until the best-fit parameters converge and the number of fit returns converges. For the binned region of figure 5(*e*) (reproduced in figure 6*b*), the fit curve and associated fit-lidar returns (curve and black dots in figure 6(*b*), respectively), capture the overturn shape well.

The lidar returns are not distributed uniformly along the overturn curve (figure 6*b*). In particular the upper-back (red, figure 6), lower-back (green), jet (magenta) and impacting front-face (brown) regions typically have fewer lidar returns, whereas the blue regions (figure 6) typically have more lidar returns. Having unsampled regions of the curve can bias the fit parameters. To prevent this, additional constraints are applied. First, we require the number of fit-lidar returns $n_{fit} > 150$. Second, we require that specific regions of the overturn curve have lidar returns associated with them. We require at least eight lidar returns associated with the front-face and lower-back regions (brown and green, respectively, in figure 6). We also require at least three lidar returns associated in the impacting jet region (magenta) and the upper-back of the overturn (magenta and red in figure 6), regions that typically have fewer returns. For example, the fit in figure 6(*b*) has five lidar returns associated with the upper-back of the overturn. Overall, there were 70 fit-snapshots across the 22 waves.

For a complete overturn, the fit process is robust and the overturn shape is well captured by the fit for many wave lidar snapshots. In figure 7, two left-wave and two right-wave examples of fit-snapshots are shown with the fit-overturn curve and fit-lidar returns applied to the $\Delta \tilde{y} = 2$ m region defining a complete overturn. For these examples, fit-lidar returns are sufficient in the lower-back, upper-back and jet regions (corresponding to green, red and magenta regions, respectively, of figure 6) of the overturn. These fit-snapshot examples (figure 7) also highlight qualitatively how cross-wave wind may affect overturning wave shape. For both left- and right-waves in offshore wind conditions $(U_w/C < 0)$, the fits give a relatively large aspect ratio $W/L \approx 0.5$ (figures 7*a*,*b*) and larger dimensional overturn
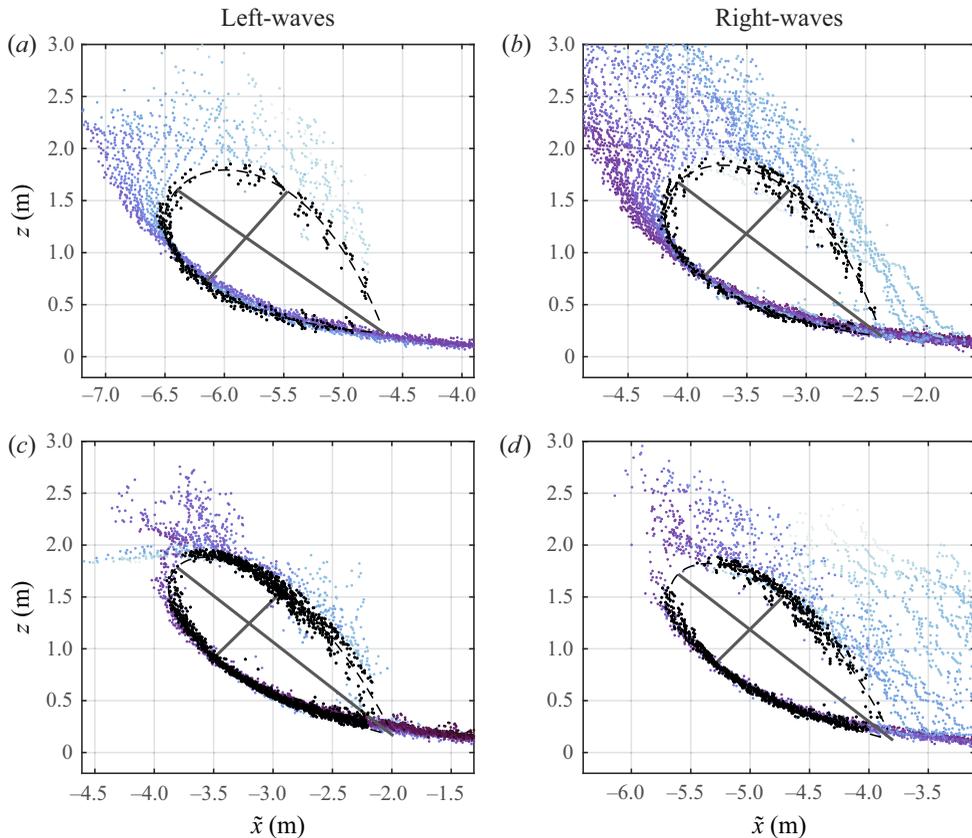
Figure 7. Examples of lidar snapshot returns (colours representing $\tilde{y}$) as a function of $\tilde{x}$ and z with fit-lidar returns (black) within the $\Delta y = 2$ m wide region of the complete overturn and the fit-overturn curve (grey dashed). Thick grey lines represent L and W. (*a,c*) Left-waves and (*b,d*) right-waves for (*a,b*) offshore wind conditions $U_w/C = \{-0.18, -0.76\}$, and (*c,d*) onshore wind conditions $U_w/C = \{0.60, 0.07\}$. The wave-overturning shape parameters are (*a*) $A = 1.74$ m^2, $W/L = 0.51$; (*b*) $A = 1.74$ m^2, $W/L = 0.49$; (*c*) $A = 1.46$ m^2, $W/L = 0.35$; (*d*) $A = 1.47$ m^2, $W/L = 0.36$. For all four panels, θ is within $\pm 2°$ of $40°$.

area $A = 1.74$ m^2. In contrast, the onshore wind ($U_w/C > 0$) cases have smaller aspect ratios $W/L \approx 0.35$ and smaller $A \approx 1.47$ m^2 than those for offshore winds. In all four cases, the fit θ was within $\pm 2°$ of $\theta = 40°$.

This fitting process is applied for each lidar snapshot of each wave where $-8 < \tilde{x}_{wf} < -3$ m. Each lidar snapshot is binned into $\Delta\tilde{y} = 2$ m wide bins (e.g. figure 5) with bin centres $\tilde{y}_c$ moving over every 0.3 m, corresponding to roughly 0.1 s of wave evolution. Smaller $\Delta\tilde{y}$ regions result in fewer fit-snapshots, and larger $\Delta\tilde{y}$ result in more aliasing of temporal wave evolution. The fit method is applied to the $\tilde{y}_c$ bins that capture a complete overturn (e.g. figure 5e). If multiple $\tilde{y}_c$ binned regions are considered fit-snapshots, then the most positive $\tilde{y}_c$ bin is used. For the 22 waves, the average number of fit-snapshots was 3.2. Four waves had only one fit-snapshot, three waves had two fit-snapshots, and the rest had more than three fit-snapshots. For each wave, mean area A (3.2) and mean aspect ratio W/L are estimated by averaging parameters across all fit-snapshots. For waves with ≥ 2 fit-snapshots, we also calculate standard errors of A and W/L from their standard deviations (σ_A, $\sigma_{W/L}$) divided by $\sqrt{n-1}$.

Figure 8. Wave and cross-wave wind parameters for the 22 analysed waves. (*a*) Wave staff wave height H versus still-water depth h, and (*b*) nonlinearity parameter H/h versus U_w/C. Red circles and blue diamonds represent left- and right-waves, respectively. In (*a*), the correlation between h and H is $r = \{0.13, 0.21, -0.03\}$ for left-waves, right-waves and all waves. In (*b*), the correlation between U_w/C and H/h is $r = \{-\mathbf{0.71}, \mathbf{0.75}, \mathbf{0.42}\}$ for left-waves, right-waves and all waves. For reference, the 95 % significance level for correlation is 0.52 for the left- or right-waves, and 0.36 for all waves. Correlations significantly (95 % level) different from zero are indicated in bold here and in the captions for figures 9, 10 and 12.

wave-overturning parameters. Note that these H/h and U_w/C correlations are significantly different from zero (figure 8*b*) but do not imply causation. These U_w/C and H/h correlations and anti-correlations for left- and right-waves are largely due to the different wind and wave generation conditions on 14 March. For all waves, the H/h and U_w/C relationship is less clear, with weaker correlation $r = 0.42$.

4.2. *Non-dimensional breakpoint location*

We now examine the effect of the non-dimensional cross-wave wind speed U_w/C and the nonlinearity parameter H/h on the non-dimensional breakpoint location $\Delta X_{bp}/\bar{L}_{sz}$ (figure 9). The location $\Delta X_{bp}/\bar{L}_{sz}$ varies as ± 0.1, with more positive (wider surf zone) $\Delta X_{bp}/\bar{L}_{sz}$ for left-waves than for right-waves. Note that the largest $\Delta X_{bp}/\bar{L}_{sz}$ is still shoreward of the rig (figure 9(*a*), magenta dashed line), and the $\Delta X_{bp}/\bar{L}_{sz}$ variation is far larger than its standard error of 0.006. A clear and consistent relationship is evident between $\Delta X_{bp}/\bar{L}_{sz}$ and U_w/C across left-waves ($r = 0.64$), right-waves ($r = 0.85$) and all waves ($r = 0.83$) with similar slopes and significant correlations (figure 9*a*). This relationship is similar to that seen in laboratory observations with stronger U_w/C magnitudes (Douglass 1990; King & Baker 1996). In contrast, the relationship between $\Delta X_{bp}/\bar{L}_{sz}$ and H/h (figure 9*b*) is scattered (lower correlation) and not consistent across left- and right-waves. For left-waves, $\Delta X_{bp}/\bar{L}_{sz}$ and H/h are negatively correlated, $r = -0.45$, opposite to the expectation that larger H/h values lead to breaking at larger cross-basin positions. The right-waves have a scattered $\Delta X_{bp}/\bar{L}_{sz}$ relationship, with moderate $r = 0.54$. For all waves, $\Delta X_{bp}/\bar{L}_{sz}$ and H/h have correlation $r = 0.49$, but the relationship lacks consistency across left- and right-waves. The consistent $\Delta X_{bp}/\bar{L}_{sz}$ relationship with U_w/C indicates that cross-wave wind has the dominant influence in our experiment with weak H/h variation. The moderate yet at times significant correlations
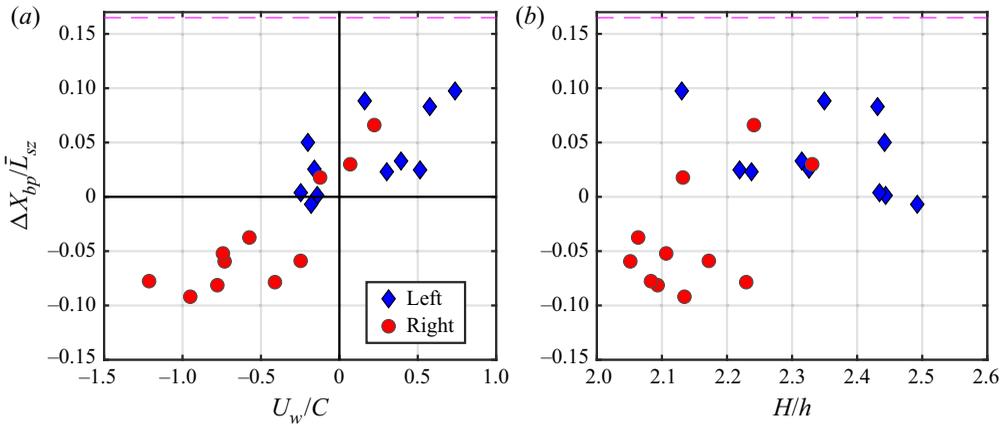
Figure 9. Non-dimensional perturbation breakpoint location $\Delta X_{bp}/\bar{L}_{sz}$ versus (*a*) non-dimensional cross-wave wind speed U_w/C, and (*b*) nonlinearity parameter H/h. Red circles and blue diamonds represent left- and right-waves, respectively. The magenta dashed line at $\Delta X_{bp}/\bar{L}_{sz} = 0.1523$ is the location of the rig. In (*a*), the thick black lines highlight zero values of abscissa and ordinate. Also, the correlations between U_w/C and $\Delta X_{bp}/\bar{L}_{sz}$ are $r = \{\mathbf{0.64}, \mathbf{0.85}, \mathbf{0.83}\}$ for left-waves, right-waves and all waves. In (*b*), the correlations between H/h and $\Delta X_{bp}/\bar{L}_{sz}$ are $r = \{-0.45, \mathbf{0.54}, \mathbf{0.49}\}$ for left-waves, right-waves and all waves. Correlations significantly (95 % level) different from zero are indicated in bold (see figure 8). Note that the standard error of $\Delta X_{bp}/\bar{L}_{sz}$ is 0.006, which is very small relative to the variation of $\Delta X_{bp}/\bar{L}_{sz}$.

between H/h and $\Delta X_{bp}/\bar{L}_{sz}$ with opposite signs for left- and right-waves is attributed to the correlations between H/h and U_w/C (figure 8*b*).

4.3. *Wave-overturn shape parameters*

Next, we focus on the non-dimensional overturning shape parameters – the area A/H^2 and the aspect ratio W/L – and the effect of both cross-wave wind U_w/C and the nonlinearity parameter H/h on them (figure 10). Across all waves, A/H^2 varies from 0.2 to 0.42, a range similar to that observed previously on different bathymetries (Blenkinsopp & Chaplin 2008; O'Dea *et al.* 2021). The area A/H^2 decreases with increasing onshore wind (increasing U_w/C, figure 10*a*). For the strongest onshore wind ($U_w/C \approx 0.75$), $A/H^2 \approx 0.2$, and $A/H^2 \approx 0.4$ for offshore wind ($U_w/C < -0.4$). For stronger offshore winds, A/H^2 appears to saturate near ≈ 0.4. The A/H^2 and U_w/C relationship is consistent for both wave directions, with significant correlations $r = \{-0.74, -0.64, -0.83\}$ for left-waves, right-waves and all waves, respectively (figure 10*a*). In contrast, the relationship between A/H^2 and H/h is not consistent across the left- and right-waves (figure 10*b*). For the left-waves, A/H^2 and H/h are positively correlated ($r = 0.67$), consistent with increased nonlinearity increasing overturn area (Blenkinsopp & Chaplin 2008). However, the right-waves have a negative correlation ($r = -0.59$), implying a sign change in the slope, inconsistent with Blenkinsopp & Chaplin (2008). The resulting correlation for all waves is also negative ($r = -0.45$). This indicates that for the observed variation in U_w/C and H/h, cross-wave wind is the dominant factor in setting overturn area. The significant yet opposite left- and right-waves signed correlations between H/h and A/H^2 are also due to the correlations between H/h and U_w/C (figure 8*b*). Finally, both A/H^2 and H/h contain H, implying that H variations alone could induce an inverse A/H^2 and H/h relationship. However, such an inverse relationship is not

958 A4-18
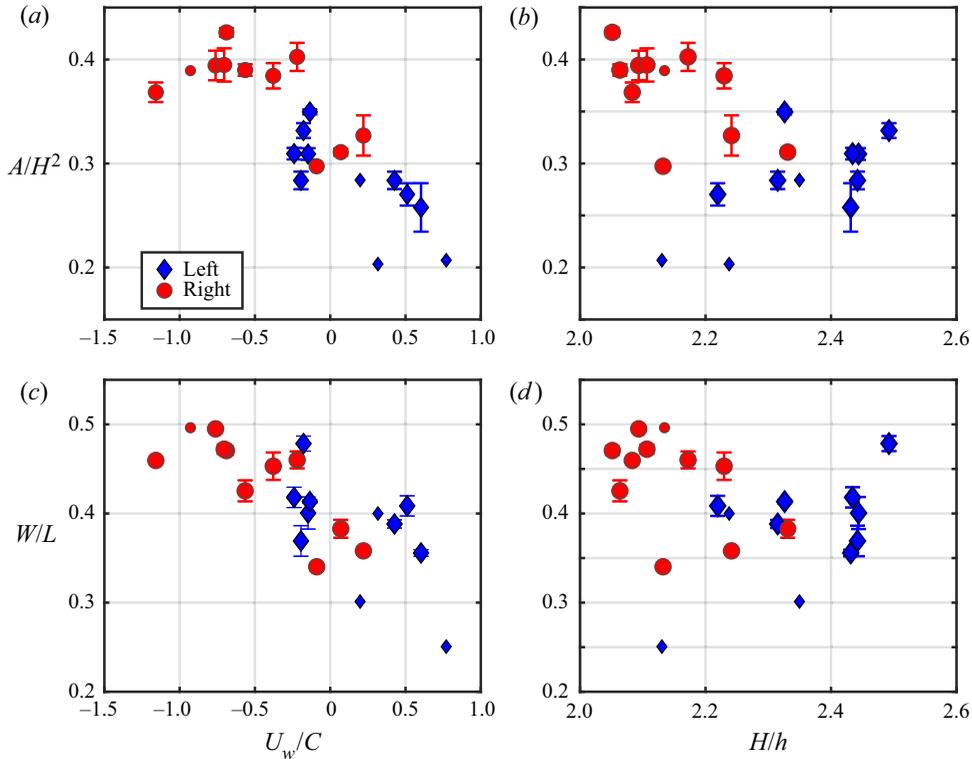
Figure 10. Non-dimensional wave-overturn area (A/H^2) and aspect ratio W/L versus (a,c) non-dimensional cross-wave wind speed U_w/C, and (b,d) H/h. Blue diamonds and red circles represent left-waves and right-waves, respectively. The symbol is the mean, and the error bar represents the standard error. The four smaller symbols represent the waves with only one fit-snapshot. The correlations between A/H^2 and U_w/C are $r = \{-0.75, -0.64, -0.83\}$ for left-waves, right-waves and all waves, whereas between A/H^2 and H/h they are $r = \{0.67, -0.59, -0.45\}$. For W/L, its correlations with U_w/C and H/h, respectively, are $r = \{-0.61, -0.80, -0.77\}$ and $r = \{0.53, -0.49, -0.25\}$ for left-waves, right-waves and all waves. Correlations significantly (95 % level) different from zero are indicated in bold (see figure 8).

observed across both left- and right-waves, indicating that a self-generated relationship is not present.

Across all waves, overturn aspect ratio W/L varies from 0.26 to 0.5, a range consistent with, albeit somewhat smaller than, previous observations (Blenkinsopp & Chaplin 2008; O'Dea *et al.* 2021). Similar to A/H^2, W/L is also a decreasing function of increasing onshore wind (figure 10c), varying from $W/L \approx 0.48$ for $U_w/C < -0.5$ to $W/L \approx 0.25$ for the strongest onshore wind $U_w/C = 0.75$. The W/L and U_w/C relationship is consistent for both wave directions, with significant correlations $r = \{-0.61, -0.80, -0.77\}$ for left-waves, right-waves and all waves, respectively. In contrast, the relationship between W/L and H/h is not consistent across the left- and right-waves (figure 10d). For the left-waves, W/L and H/h are positively correlated ($r = 0.53$), yet for the right-waves they are negatively correlated ($r = -0.47$), implying a sign change in the slope that is attributed to the sign change in the U_w/C and H/h correlation for left- and right-waves (figure 8b). The resulting W/L and H/h correlation for all waves is weak ($r = 0.25$). For the observed variation in U_w/C and H/h, the consistent relationship of A/H^2 or W/L with U_w/C across both left- and right-waves, together with the inconsistent

relationship with H/h and the H/h and U_w/C correlation, indicates that U_w/C is the dominant factor controlling the wave-overturning parameters in our experiment.

5. Discussion

5.1. *Contextualizing with prior results*

We have shown that cross-wave winds have a significant effect on wave breakpoint location and overturning shape for field-scale shoaling solitons on fixed bathymetry with small wave height variations. The effect of cross-wave winds dominates that of along-wave (transverse) winds. The range of the non-dimensional cross-wave wind speed ($-1.2 < U_w/C < 0.7$) was realistic for natural surf zone conditions. Here, we contextualize our results with those of Blenkinsopp & Chaplin (2008) and O'Dea *et al.* (2021). The Blenkinsopp & Chaplin (2008) laboratory experiments were in still air ($U_w = 0$) and had progressive waves shoaling on triangular bathymetry (constant β) with variable minimum depth h_c that immediately farther shoreward falls off to deeper water. Blenkinsopp & Chaplin (2008) used H_0/h_c as a nonlinearity parameter, where H_0 was the equivalent deep-water wave height, and H_0/h_c varied from 0.625 to 1.25, a factor of 2 variation, significantly larger than our factor 1.2 variation in H/h. The differences in wave types, bathymetry and data metrics make quantitative comparison challenging. Nevertheless, a few points can be made. First, Blenkinsopp & Chaplin (2008) observed an equivalent of A/H^2 varying from 0.05 to 0.35, similar to our A/H^2 variations of 0.2–0.4 (figure 10). However, the Blenkinsopp & Chaplin (2008) A/H^2 variation occurred over a large H_0/h_c range, whereas we had similarly large A/H^2 variations for a much smaller H/h range. This is consistent with our conclusion that U_w/C is driving A/H^2 variability. Second, Blenkinsopp & Chaplin (2008) observed W/L to vary from 0.43 to 0.67, larger than our values (0.26–0.5). Yet they found no nonlinearity parameter dependence on W/L. This is also consistent with our conclusion that U_w/C is driving W/L variations in our experiment.

O'Dea *et al.* (2021) observed wave overturning on three distinct days with variable bathymetry profiles (from planar to barred), random directionally spread incident waves, and wind. They observed an equivalent A/H^2 variation of 0.05–0.3, on average smaller than our values, that increased with local β, qualitatively consistent with potential flow BEM results (Grilli, Svendsen & Subramanya 1997). O'Dea *et al.* (2021) also showed that A/H^2 decreased for larger-dimensional breaking water depths h_b (varying from 2 m to 3 m), qualitatively (but not dimensionally) consistent with Blenkinsopp & Chaplin (2008), although β and h_b also appear correlated, particularly across days. The Surf Ranch analogues of β and h_b were essentially constant, again consistent with our conclusions that U_w/C is strongly affecting A/H^2. O'Dea *et al.* (2021) observed that the aspect ratio W/L varied from 0.32 to 0.59, somewhat larger than our values (figure 10), and was inversely dependent on $\beta(kh)$, where kh is the non-dimensional water depth at breaking, and k is the wavenumber. An analogous soliton-based parameter in our study is essentially constant. O'Dea *et al.* (2021) also found that W/L was larger (smaller) for offshore (onshore) wind, consistent with our results. However, the inferred U_w/C values were somewhat weaker ($\sim \pm 0.5$) and correlation was lower ($|r| = 0.45$). In addition, cross-correlation between parameters was not taken into account. In sum, the realistic observed cross-wave wind variations with small H/h variations made the strong U_w/C effects on wave-overturning parameters clear. If the H/h variations had been large (as in Blenkinsopp & Chaplin 2008), then it likely also would have had an impact on wave-overturning parameters.

Our somewhat smaller aspect ratios W/L relative to Blenkinsopp & Chaplin (2008) and O'Dea *et al.* (2021) may be explained by the difference in progressive waves and solitons. In a fixed reference frame, the soliton horizontal water velocities u are always positive, in the direction of wave propagation. Thus the water level in front of the soliton is not depressed due to the lack of negative u. However, for progressive waves, u has both signs. As wave amplitude gets large, negative u/C will get large in front of the wave crest, as noted by Blenkinsopp & Chaplin (2008). As these progressive waves become very steep, the large negative velocities may draw enough water off the reef in front of the wave to depress the local breaking water depth or influence wave overturning nonlinearly. This may lead to larger aspect ratios for progressive waves relative to solitons.

5.2. *Limitations*

Here, we discuss some limitation of our study. The wind measurements were 16 m above the water surface, may have had some veering, and were not corrected to the surface. The Surf Ranch bathymetry was fixed and the incident solitons were similar. Natural beaches and reefs have variable non-planar bathymetry, tides inducing significant water depth changes, and random directionally spread progressive waves. The Surf Ranch is also extremely fetch limited. Natural settings are usually not fetch limited for onshore winds. Locally generated short wind-waves riding on longer strongly shoaling and overturning waves may lead to incipient wave breaking under certain conditions (Mailybaev & Nachbin 2019), likely affecting wave-overturning parameters. Furthermore, we are using the local parameter H/h to represent nonlinear effects on the wave-overturning parameters. For given incident waves, the entirety of wave shoaling on a bathymetry determines wave shape and the geometric properties of the wave overturn. Thus parametrizing shoaling wave skewness and asymmetry purely in terms of local wave and bathymetric properties is challenging (Elfrink, Hanes & Ruessink 2006). The integral property of shoaling-wave evolution is most clearly seen for a soliton shoaling on a planar slope, where wave height scales with h^{-r}, and r depends on bathymetric slope β and wave nonlinearity. In particular, $r = 1$ for very mild β but strong nonlinearity (Miles 1979), $r = 1/4$ for small β and weak nonlinearity (Green's law), and $r < 1/4$ for steep β and finite nonlinearity (Knowles & Yeh 2018). Cross-wave wind also has an integral effect on wave shape during shoaling (Zdyrski & Feddersen 2022). Therefore, this local parameter can only represent in bulk the integrated effects of wave shoaling, and is unlikely to be a good metric across a range of bathymetries and incident wave conditions. Finally, although our results clearly demonstrate a strong cross-wave wind effect on overturning wave shape, we do not present a curve fit or parametrization of A/H^2 or W/L based on U_w/C, as that would be specific to the bathymetry, solitons and winds during our experiment.

5.3. *Mechanism*

Here, we discuss the mechanism for the cross-wind-induced changes to overturning wave shape. Wind and wave interactions are well studied and continue to be an important research topic, with focus on open ocean wind-wave generation, wave breaking, and fluxes of energy, momentum, heat and gas (e.g. Deike 2022). In studies of wind-induced wave generation, the focus is often on deep-water linear periodic waves with relatively small wave slopes (< 0.25) and relatively strong winds, i.e. $U_w > C$ (e.g. Husain *et al.* 2019). Recent studies with 'offshore' winds and similar waves show that the surface pressure perturbation is relatively large and $180°$ out of phase with the wave surface (e.g. Cao,
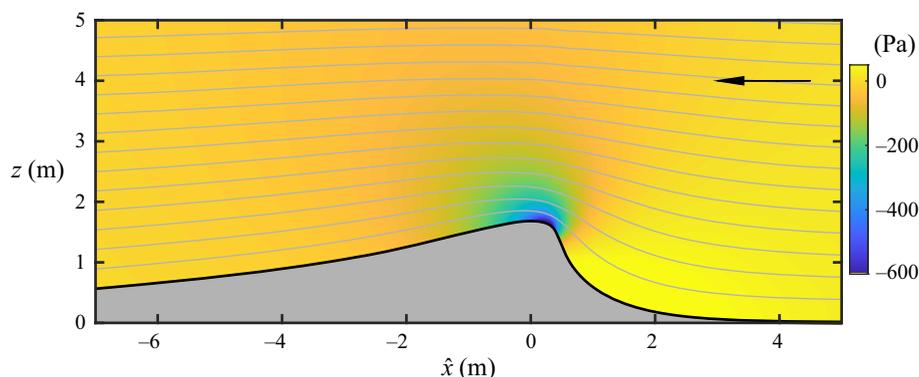
Figure 11. Snapshot of a static profile based on a modelled shoaling soliton just prior to overturning (grey and black outline) versus a cross-wave coordinate $\hat{x}$. The maximum surface-slope magnitude is 70°. Potential flow modelled air perturbation dynamic pressure P_d (Pa, coloured) and wind streamlines (lines) as a function of $\hat{x}$ and z for upstream free-stream wind of -14.8 m s^{-1} corresponding to offshore wind at $U_w/C = -1$. The black arrow denotes the direction of the upstream wind. The vertical domain extends to $z = 20$. Only a small portion of the horizontal domain is shown, to highlight the near-crest region.

Deng & Shen 2020; Husain, Hara & Sullivan 2022). A range of large-eddy simulations (LES) and DNS shows that at the wave surface, the pressure forces are much larger than the viscous forces (Sullivan *et al.* 2018; Husain *et al.* 2019; Hao, Cao & Shen 2021), and the pressure contribution increases with larger wave slope (Sullivan *et al.* 2018; Wu, Popinet & Deike 2022). Note that here, the wave slope is large both at the hydrofoil where $H/h \approx 0.8$ and at shoaling and overturning where the slope is ≥ 1 (e.g. figures 4 and 5). Thus we infer that wind-induced surface pressure forcing through the surface dynamic boundary conditions leads to the observed changes in the overturning wave shape.

To investigate properly the physical processes of how wind affects depth-limited wave overturning, a high-resolution multi-phase model (e.g. Mostert & Deike 2020) is required. Here, we assess qualitatively the changes in surface pressure induced by offshore wind with potential flow modelling of air over a fixed obstacle analogous to a steeply shoaling soliton. First, a one-dimensional potential-flow BEM is run for an initial soliton shoaling on the Surf Ranch bathymetry projected into the observed angle of propagation. A very steep wave profile (with maximum slope 70°) just prior to overturning is extracted (grey region of figure 11) and is assumed to be fixed. The cross-wave coordinate system has $\hat{x} = 0$ at the crest. The steady potential air flow (free-slip boundary conditions) over this obstacle is modelled with a BEM code around this fixed obstacle for the equivalent of offshore wind $U_w/C = -1$ for a wave propagating at speed $+C$. In a coordinate system where the obstacle is fixed, the equivalent free-stream air flow is $-2C$ (or -14.8 m s^{-1}). Once Laplace's equation is solved for the air velocity potential ϕ_a, the steady perturbation dynamic pressure P_d is solved for, with

$$P_d = -\tfrac{1}{2}\rho_a \left|\nabla \phi_a\right|^2 - P_{d,0}, \tag{5.1}$$

where $\rho_a = 1.23$ kg m^{-3} is the density of air, and $P_{d,0}$ is the inflow dynamic air pressure associated with wind at -14.8 m s^{-1}. We also calculate the steady streamfunction by vertically integrating $-\partial \phi_a/\partial \hat{x}$ from the wave surface.

In front of the wave-like obstacle ($\hat{x} \approx 5$ m, figure 11), the surface slopes gently, the nearby air streamlines are evenly spaced and are largely horizontal with wind speed

958 A4-22

slightly reduced from the upstream value, and the surface $P_d = 22$ Pa is positive and weak. On the front face of the wave-like obstacle (figure 11), the water surface slopes up and the streamlines are more separated, indicating slowing air flow, increasing the surface dynamic pressure to $P_d \approx 88$ Pa at $\hat{x} = 1.2$ m. Near the wave crest ($\hat{x} = 0$), the air flow accelerates (streamlines converge), with velocity increased by a factor 2.5, which decreases P_d substantially within 1 m in the vertical and horizontal of the wave crest (figure 11). Analogous streamline convergence is also seen in LES of wind over steady wave surfaces (Husain *et al.* 2022). The minimum surface $P_d = -744$ Pa is located just in front of the wave crest at $\hat{x} = 0.3$ m. Farther behind the wave, the surface P_d increases and returns to the background level. On the front face of the wave, the surface P_d varies by $\Delta P_d = 832$ Pa over a relatively short distance $\Delta \hat{x} = 0.89$ m. This suggests that the wind-induced surface pressure changes can impact the shape of wave overturning. We can evaluate this surface pressure change within the wave dynamic boundary condition. Using water density $\rho_w = 1025$ kg m^{-3} and gravity 9.81 m s^{-2}, this pressure change is equivalent to a hydrostatic water elevation change 0.08 m, which 5 % of the wave elevation, and is thus significant. The high pressure located at the base of the wave face would slightly retard wave velocities normal to the surface, and the strong low pressure near the crest would accelerate outward-normal velocities near the crest, potentially explaining the larger overturn areas and aspect ratios. Note that in this idealized setting for onshore wind with $U_w/C = 1$, $\Delta P_d = 0$ everywhere along the surface.

Although this simulation has limitations, it clearly highlights the air flow acceleration near the wave crest and the strength of wind-induced surface pressure variations for very steep nearly overturning waves. As a wave steepens further, these surface pressure variations should only increase. Modelling limitations include assuming steady flow, whereas the wave and air evolve very rapidly. For unsteady wave fields, form drag is elevated relative to steady waves of the same steepness (Sullivan *et al.* 2018), indicating larger perturbation pressures in evolving waves, such as shoaling and overturning waves. In addition, for small wave slopes, velocities normal to the surface affect air velocity and pressure (e.g. Cao *et al.* 2020; Stokes & Lucas 2021). This effect is likely even larger for steep waves. However, surface-normal air velocity is assumed zero here. Potential air flow is assumed throughout. Yet it is clear from the surface pressure distribution that flow separation will occur in the lee if the no-slip boundary conditions are satisfied (e.g. Sullivan *et al.* 2018). In fact, for offshore wind, flow separation is clear from the spray ejected behind the wave as overturning is about to begin, as seen in figure 2(*b*) and in the lidar returns (figure 4). However, the air flow could be assumed reasonably laminar up to the crest where the largest pressure variations occur. Future work will examine the cross-wave wind effect on wave shape both in shoaling and overturning using two-phase numerical models.

5.4. *Significance*

As mentioned in the Introduction, overturning wave shape is known to affect processes associated with wave breaking such as bubble entrainment and turbulence injection. The induced sediment suspension and transport is one of the most important resulting processes affected by depth-limited wave breaking (Aagaard *et al.* 2021). Wave skewness and asymmetry are well understood to affect sediment transport (e.g. Hoefel & Elgar 2003). During wave shoaling, these parameters are affected by wind in laboratory observations (Feddersen & Veron 2005) and models (Zdyrski & Feddersen 2021). Plunging versus spilling wave breaking is understood to affect local water column

turbulence (e.g. Ting & Kirby 1995, 1996) and sediment suspension (e.g. Aagaard *et al.* 2018). The cross-shore distribution of depth-integrated wave energy dissipation D_w is also important to cross-shore and along-shore surf zone current distributions (e.g. Ruessink *et al.* 2001; Kumar *et al.* 2012). From this and previous studies (Douglass 1990; King & Baker 1996; Feddersen & Veron 2005; Blenkinsopp & Chaplin 2008; O'Dea *et al.* 2021), we can infer that onshore wind leads to changes in shoaling wave skewness and asymmetry, as well as wider surf zones, lower average D_w, and smaller, less-energetic overturns leading to reduced water column turbulence and less sediment suspension. In contrast, offshore wind leads to different shoaling skewness and asymmetry, as well as narrower surf zones, larger average D_w, energetic overturns with strong turbulence injection, and increased sediment suspension. Thus these wind effects are likely important in near-shore sediment transport and beach morphology evolution. However, very few near-shore wave models (essentially two-phase DNS and LES) could incorporate wind effects. Neglecting wind effects may contribute to the weak skill of models simulating beach morphological evolution (Montaño *et al.* 2020). Different beaches around the world experience different types of wind conditions. Many continental regions have different magnitudes of diurnal sea breezes (Gille, Llewellyn Smith & Statom 2005), synoptic scale and seasonal wind variability. Thus the local wind climate possibly could be a determining factor for the beach morphological conditions, such as whether the beach is barred or not. Many factors control beach morphological change, and although linking beach morphology variability to wind climate is speculative, investigating such connections may bear fruit.

6. Summary

Here, field-scale wave-overturning observations from the Kelly Slater Wave Company's Surf Ranch are used to study cross-shore wind effects on the location and shape (area and aspect ratio) of wave overturning. The Surf Ranch bathymetry was fixed with obliquely incident shoaling solitons with height ≈ 2.25 m that varied weakly. Both left-waves and right-waves were generated in sequence. Winds were observed from a meteorological station located 16 m above the still-water surface. The shoaling and overturning waves were observed in the centre of the wave basin using georectified UAV images, a wave staff, and a 32-beam lidar mounted 4 m above the water surface above the wave staff. A total of 22 waves (11 left-waves and 11 right-waves) passed quality control criteria. For each wave, the cross-shore breakpoint location X_{bp} as well as the mean surf zone width $\bar{L}_{sz}$ were estimated from the georectified images. Wave staff observations are used to estimate the wave height H and local water depth h. Lidar data rotated into a cross-wave and along-wave coordinate system clearly visualize the wave overturn. Observed non-dimensional cross-wave wind was both onshore and offshore, and varied realistically ($-1.2 < U_w/C < 0.7$). For each wave, overturn area A and aspect ratio W/L were estimated by first selecting lidar returns that represent the along-wave region of a complete overturn, iteratively fitting returns to a parametric functional form, and subsequently averaging parameters over all wave lidar snapshots that pass fitting criteria.

We test the hypothesis that cross-wave wind direction and magnitude affect non-dimensional breakpoint location $\Delta X_{bp}/\bar{L}_{sz}$, overturn area A/H^2 and aspect ratio W/L – specifically, that $\Delta X_{bp}/\bar{L}_{sz}$ increases with U_w/C, and A/H^2 and W/L decrease with U_w/C. As wave nonlinearity, through H/h, can also impact the wave-overturning parameters, we explore their relationship to both U_w/C and H/h. The wave staff H and

h both varied weakly and were uncorrelated, indicating that wave height variations are not linked to wave basin seiching. The nonlinearity parameter H/h varied weakly and had opposite-signed correlations with U_w/C for the two wave directions. The non-dimensional $\Delta X_{bp}/\bar{L}_{sz}$ was inversely related to U_w/C, similar to previous laboratory experiments with much stronger winds, and did not consistently depend on H/h across combined left- and right-waves. The non-dimensional overturn area A/H^2 and aspect ratio W/L also were inversely related to U_w/C, with smaller and narrower overturns for increasing onshore wind. At stronger offshore winds, A/H^2 appears to saturate. No overturning area or aspect ratio dependence on weakly-varying H/h was seen across left- and right-waves combined. The wind-induced overturning wave A/H^2 and W/L variations was as large as prior laboratory experiments with strong H/h variations without wind. This demonstrates that cross-wave wind direction and magnitude have a strong effect on the size and aspect ratio of wave overturns in our experiment. Incorporating wind effects on wave overturning requires a two-phase LES or DNS model. Idealized potential air flow simulations on steep shoaling soliton shapes indicate strong wave surface pressure variations that likely induce overturning shape changes. As wave-overturning shape impacts turbulence, bubble entrainment and sediment suspension, cross-shore wind may lead to downstream effects on sediment transport and beach morphology.

Author ORCIDs.

Falk Feddersen https://orcid.org/0000-0002-5488-9074;

Katherine L. Brodie https://orcid.org/0000-0003-1945-5112;

Adam P. Young https://orcid.org/0000-0001-7985-9528;

M.S. Spydell https://orcid.org/0000-0002-7861-792X;

Derek J. Grimes https://orcid.org/0000-0001-5286-7819;

Kentaro Hanson https://orcid.org/0000-0002-0468-226X.

Appendix. Effect of along-wave (transverse) wind on wave-overturn shape

In the Results section (§ 4), we showed that the non-dimensional cross-wave wind U_w/C had a significant effect on the breakpoint location and overturning wave shape parameters (figures 9a and 10a,c). Realistic winds typically have both cross-wave and along-wave (i.e. blowing into or away from the overturn) components. A potential alternative hypothesis is that the along-wave wind affects overturning wave shape. Similar to the cross-wave wind (U_w), the along-wave wind V_w is estimated by taking the dot product of the observed wind with $\tilde{y}$, where $V_w < 0$ is wind blowing into the overturn, and $V_w > 0$ is wind blowing away from the overturn (figure 3). We non-dimensionalize using C, the wave
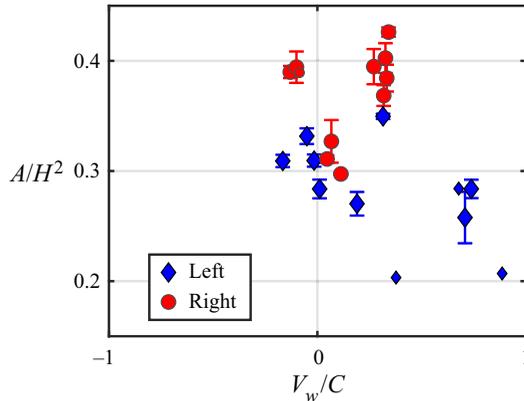
Figure 12. Non-dimensional wave-overturn area (A/H^2) versus non-dimensional along-wave (transverse) wind speed V_w/C. Blue diamonds and red circles represent left-waves and right-waves, respectively. The symbol is the mean, and the error bar represents the standard error. The four smaller symbols represent the waves with only one fit-snapshot. The correlations between A/H^2 and V_w/C are $r = \{-\mathbf{0.56}, 0.23, -\mathbf{0.43}\}$ for left-waves, right-waves and all waves. For reference, 95 % significance for correlation is 0.27 for the left- or right-waves.

velocity in the $+\tilde{x}$ direction, allowing direct comparison of cross- and along-wave wind magnitudes. Normalizing with the wave velocity in the $\tilde{y}$ direction, $C_{\tilde{y}} = 3.19\text{m s}^{-1}$, yields similar results, as both C and $C_{\tilde{y}}$ are constant (§ 3.2). The V_w/C range (figure 12) is similar to that of U_w/C, although because $+\tilde{y}$ points towards the tram for both left- and right-waves, most V_w/C values are positive, in contrast to U_w/C values (figure 10a). The relationship of A/H^2 with V_w/C is weaker than that with U_w/C (compare figures 12 and 10a). Furthermore, the A/H^2 and V_w/C relationship is inconsistent across left-waves and right-waves as the sign of the correlation switches and only the left-wave correlation is significant. Similar results are seen for aspect ratio as well (not shown). This shows that although along-wave (transverse) winds may have an effect on overturning wave shape, the cross-wave winds are the dominant wind component in setting overturning wave shape.

REFERENCES

AAGAARD, T., BRINKKEMPER, J., CHRISTENSEN, D.F., HUGHES, M.G. & RUESSINK, G. 2021 Surf zone turbulence and suspended sediment dynamics; a review. *J. Mar. Sci. Engng* **9** (11), 1300.
AAGAARD, T., HUGHES, M.G. & RUESSINK, G. 2018 Field observations of turbulence, sand suspension, and cross-shore transport under spilling and plunging breakers. *J. Geophys. Res.: Earth Surf.* **123** (11), 2844–2862.
BLENKINSOPP, C.E. & CHAPLIN, J.R. 2007 Void fraction measurements in breaking waves. *Proc. R. Soc. Lond.* A*: Math. Phys. Engng Sci.* **463** (2088), 3151–3170.
BLENKINSOPP, C.E. & CHAPLIN, J.R. 2008 The effect of relative crest submergence on wave breaking over submerged slopes. *Coast. Engng* **55** (12), 967–974.
BRODIE, K.L., RAUBENHEIMER, B., ELGAR, S., SLOCUM, R.K. & MCNINCH, J.E. 2015 Lidar and pressure measurements of inner-surfzone waves and setup. *J. Atmos. Ocean. Technol.* **32** (10), 1945–1959.
BRUDER, B.L. & BRODIE, K.L. 2020 CIRN Quantitative Coastal Imaging Toolbox. *SoftwareX* **12**, 100582.
BULLOCK, G.N., OBHRAI, C., PEREGRINE, D.H. & BREDMOSE, H. 2007 Violent breaking wave impacts. Part 1: results from large-scale regular wave tests on vertical and sloping walls. *Coast. Engng* **54** (8), 602–617.
CAO, T., DENG, B.-Q. & SHEN, L. 2020 A simulation-based mechanistic study of turbulent wind blowing over opposing water waves. *J. Fluid Mech.* **901**, A27.

CARINI, R.J., CHICKADEL, C.C. & JESSUP, A.T. 2021 Surf zone waves at the onset of breaking: 1. Lidar and IR data fusion methods. *J. Geophys. Res.: Oceans* **126** (4), e2020JC016934.

CHANSON, H. & JAW-FANG, L. 1997 Plunging jet characteristics of plunging breakers. *Coast. Engng* **31** (1), 125–141.

DEIKE, L. 2022 Mass transfer at the ocean–atmosphere interface: the role of wave breaking, droplets, and bubbles. *Annu. Rev. Fluid Mech.* **54** (1), 191–224.

DEIKE, L., MELVILLE, W.K. & POPINET, S. 2016 Air entrainment and bubble statistics in breaking waves. *J. Fluid Mech.* **801**, 91–129.

DERAKHTI, M. & KIRBY, J.T. 2014 Bubble entrainment and liquid–bubble interaction under unsteady breaking waves. *J. Fluid Mech.* **761**, 464–506.

DERAKHTI, M., KIRBY, J.T., BANNER, M.L., GRILLI, S.T. & THOMSON, J. 2020 A unified breaking onset criterion for surface gravity water waves in arbitrary depth. *J. Geophys. Res.* **125** (7), e2019JC015886.

DOUGLASS, S.L. 1990 Influence of wind on breaking waves. *J. Waterways Port Coast. Ocean Engng* **116** (6), 651–663.

ELFRINK, B., HANES, D.M. & RUESSINK, B.G. 2006 Parameterization and simulation of near bed orbital velocities under irregular waves in shallow water. *Coast. Engng* **53** (11), 915–927.

ELGAR, S. & GUZA, R.T. 1985 Observations of bispectra of shoaling surface gravity waves. *J. Fluid Mech.* **161**, 425–448.

FEDDERSEN, F. & VERON, F. 2005 Wind effects on shoaling wave shape. *J. Phys. Oceanogr.* **35** (7), 1223–1228.

GILLE, S.T., LLEWELLYN SMITH, S.G. & STATOM, N.M. 2005 Global observations of the land breeze. *Geophys. Res. Lett.* **32** (5), L05605.

GRILLI, S.T., SVENDSEN, I.A. & SUBRAMANYA, R. 1997 Breaking criterion and characteristics for solitary waves on slopes. *J. Waterways Port Coast. Ocean Engng* **123** (3), 102–112.

GUYENNE, P. & GRILLI, S.T. 2006 Numerical study of three-dimensional overturning waves in shallow water. *J. Fluid Mech.* **547**, 361–388.

HAO, X., CAO, T. & SHEN, L. 2021 Mechanistic study of shoaling effect on momentum transfer between turbulent flow and traveling wave using large-eddy simulation. *Phys. Rev. Fluids* **6**, 054608.

HOEFEL, F. & ELGAR, S. 2003 Wave-induced sediment transport and sandbar migration. *Science* **299** (5614), 1885–1887.

HUSAIN, N.T., HARA, T., BUCKLEY, M.P., YOUSEFI, K., VERON, F. & SULLIVAN, P.P. 2019 Boundary layer turbulence over surface waves in a strongly forced condition: LES and observation. *J. Phys. Oceanogr.* **49** (8), 1997–2015.

HUSAIN, N.T., HARA, T. & SULLIVAN, P.P. 2022 Wind turbulence over misaligned surface waves and air–sea momentum flux. Part I: waves following and opposing wind. *J. Phys. Oceanogr.* **52** (1), 119–139.

JEFFREYS, H. 1925 On the formation of water waves by wind. *Proc. R. Soc. Lond.* A **107** (742), 189–206.

KING, D.M. & BAKER, C.J. 1996 Changes to wave parameters in the surf zone due to wind effects. *J. Hydraul. Res.* **34** (1), 55–76.

KNOWLES, J. & YEH, H. 2018 On shoaling of solitary waves. *J. Fluid Mech.* **848**, 1073–1097.

KUMAR, N., VOULGARIS, G., WARNER, J.C. & OLABARRIETA, M. 2012 Implementation of the vortex force formalism in the coupled ocean–atmosphere–wave–sediment transport (COAWST) modeling system for inner shelf and surf zone applications. *Ocean Model.* **47**, 65–95.

LAGARIAS, J.C., REEDS, J.A., WRIGHT, M.H. & WRIGHT, P.E. 1998 Convergence properties of the Nelder–Mead simplex method in low dimensions. *SIAM J. Optim.* **9** (1), 112–147.

LEYKIN, I.A., DONELAN, M.A., MELLEN, R.H. & MCLAUGHLIN, D.J. 1995 Asymmetry of wind waves studied in a laboratory tank. *Nonlinear Process. Geophys.* **2** (3/4), 280–289.

LONGUET-HIGGINS, M.S. 1982 Parametric solutions for breaking waves. *J. Fluid Mech.* **121**, 403–424.

LUBIN, P., VINCENT, S., ABADIE, S. & CALTAGIRONE, J.-P. 2006 Three-dimensional large eddy simulation of air entrainment under plunging breaking waves. *Coast. Engng* **53** (8), 631–655.

MAILYBAEV, A.A. & NACHBIN, A. 2019 Explosive ripple instability due to incipient wave breaking. *J. Fluid Mech.* **863**, 876–892.

MARTINS, K., BLENKINSOPP, C.E., DEIGAARD, R. & POWER, H.E. 2018 Energy dissipation in the inner surf zone: new insights from lidar-based roller geometry measurements. *J. Geophys. Res.: Oceans* **123** (5), 3386–3407.

MARTINS, K., BLENKINSOPP, C.E., POWER, H.E., BRUDER, B., PULEO, J.A. & BERGSMA, E.W.J. 2017 High-resolution monitoring of wave transformation in the surf zone using a lidar scanner array. *Coast. Engng* **128**, 37–43.

MCCOWAN, J. 1894 On the highest wave of permanent type. *Lond. Edinb. Dublin Phil. Mag. J. Sci.* **38** (233), 351–358.

MEAD, S. & BLACK, K. 2001 Predicting the breaking intensity of surfing waves. *J. Coast. Res.* **10**, 51–65.

MILES, J.W. 1957 On the generation of surface waves by shear flows. *J. Fluid Mech.* **3** (2), 185–204.

MILES, J.W. 1979 On the Korteweg–de Vries equation for a gradually varying channel. *J. Fluid Mech.* **91** (1), 181–190.

MONTAÑO, J., *et al.* 2020 Blind testing of shoreline evolution models. *Sci. Rep.* **10** (1), 2137.

MOSTERT, W. & DEIKE, L. 2020 Inertial energy dissipation in shallow-water breaking waves. *J. Fluid Mech.* **890**, A12.

NEW, A.L. 1983 A class of elliptical free-surface flows. *J. Fluid Mech.* **130**, 219–239.

O'DEA, A., BRODIE, K. & ELGAR, S. 2021 Field observations of the evolution of plunging-wave shapes. *Geophys. Res. Lett.* **48** (16), e2021GL093664.

PEREGRINE, D.H. 1983 Breaking waves on beaches. *Annu. Rev. Fluid Mech.* **15** (1), 149–178.

PHILLIPS, O.M. 1957 On the generation of waves by turbulent wind. *J. Fluid Mech.* **2** (5), 417–445.

PRESS, W.H., FLANNERY, B.P., TEUKOLSKY, S.A. & VETTERING, W.T. 1988 *Numerical Recipes in C*. Cambridge University Press.

RUESSINK, B.G., MILES, J.R., FEDDERSEN, F., GUZA, R.T. & ELGAR, S. 2001 Modeling the alongshore current on barred beaches. *J. Geophys. Res.* **106**, 22451–22463.

SOUS, D., FORSBERG, P.L., TOUBOUL, J. & GONÇALVES NOGUEIRA, G. 2021 Laboratory experiments of surf zone dynamics under on- and offshore wind conditions. *Coast. Engng* **163**, 103797.

STOKES, I.A. & LUCAS, A.J. 2021 Wave-slope soaring of the brown pelican. *Mov. Ecol.* **9**, 13.

SULLIVAN, P.P., BANNER, M.L., MORISON, R.P. & PEIRSON, W.L. 2018 Turbulent flow over steep steady and unsteady waves under strong wind forcing. *J. Phys. Oceanogr.* **48** (1), 3–27.

THOMPSON, C.F., YOUNG, A.P. & DICKSON, M.E. 2019 Wave impacts on coastal cliffs: do bigger waves drive greater ground motion? *Earth Surf. Process. Landf.* **44** (14), 2849–2860.

THORNTON, E.B. & GUZA, R.T. 1983 Transformation of wave height distribution. *J. Geophys. Res.* **88** (C10), 5925–5938.

TING, F.C.K. & KIRBY, J.T. 1995 Dynamics of surf-zone turbulence in a strong plunging breaker. *Coast. Engng* **24** (3–4), 177–204.

TING, F.C.K. & KIRBY, J.T. 1996 Dynamics of surf-zone turbulence in a spilling breaker. *Coast. Engng* **27** (3–4), 131–160.

VARING, A., FILIPOT, J.-F., GRILLI, S., DUARTE, R., ROEBER, V. & YATES, M. 2021 A new definition of the kinematic breaking onset criterion validated with solitary and quasi-regular waves in shallow water. *Coast. Engng* **164**, 103755.

VOULGARIS, G. & COLLINS, M.B. 2000 Sediment resuspension on beaches: response to breaking waves. *Mar. Geol.* **167** (1), 167–187.

WU, J., POPINET, S. & DEIKE, L. 2022 Revisiting wind wave growth with fully coupled direct numerical simulations. *J. Fluid Mech.* **951**, A18.

XIE, Z. 2014 Numerical modelling of wind effects on breaking solitary waves. *Eur. J. Mech. (B/Fluids)* **43**, 135–147.

XIE, Z. 2017 Numerical modelling of wind effects on breaking waves in the surf zone. *Ocean Dyn.* **67** (10), 1251–1261.

YASUDA, T., MUTSUDA, H. & MIZUTANI, N. 1997 Kinematics of overturning solitary waves and their relations to breaker types. *Coast. Engng* **29** (3), 317–346.

YASUDA, T., MUTSUDA, H., MIZUTANI, N. & MATSUDA, H. 1999 Relationships of plunging jet size to kinematics of breaking waves with spray and entrained air bubbles. *Coast. Engng J.* **41** (3-4), 269–280.

ZDYRSKI, T. & FEDDERSEN, F. 2020 Wind-induced changes to surface gravity wave shape in deep to intermediate water. *J. Fluid Mech.* **903**, A31.

ZDYRSKI, T. & FEDDERSEN, F. 2021 Wind-induced changes to surface gravity wave shape in shallow water. *J. Fluid Mech.* **913**, A27.

ZDYRSKI, T. & FEDDERSEN, F. 2022 Wind-induced changes to shoaling surface gravity wave shape. *Phys. Rev. Fluids* **7**, 074802.